Nano Research

ISSN 1998-0124 CN 11-5974/O4
https://doi.org/10.26599/NR.2026.94908679

Research Article

From PBA nanocubes to octa-truncated cubes: The ammonium oxalate etching route for enhanced performance in aqueous Ni-Zn batteries

Yue Chen[1,2], Yichun Su[3,4], Mohsen Shakouri[5], Bin He[6], Huan Pang[1](✉)

[1] School of Chemistry and Materials, Yangzhou University, Yangzhou 225002, China

[2] Interdisciplinary Research Center for Advanced Energy, Yangzhou University, Yangzhou 225127, China

[3] School of Chemistry and Chemical Engineering, Chongqing University of Science and Technology, Chongqing 401331, China

[4] School of Environmental Science, Nanjing Xiaozhuang University, Nanjing 211171, China

[5] Canadian Light Source Inc., University of Saskatchewan, Saskatoon S7N 2V3, Canada

[6] Zhejiang Key Laboratory for Industrial Solid Waste Thermal Hydrolysis Technology and Intelligent Equipment, Huzhou Key Laboratory of Environmental Functional Materials and Pollution Control, Department of Materials Engineering, Huzhou University, Huzhou 313000, China

Nano Res., **Just Accepted Manuscript** • https://doi.org/10.26599/NR.2026.94908679

https://www.sciopen.com/journal/1998-0124 on Mar. 25, 2026

Just Accepted

TABLE OF CONTENTS (TOC)

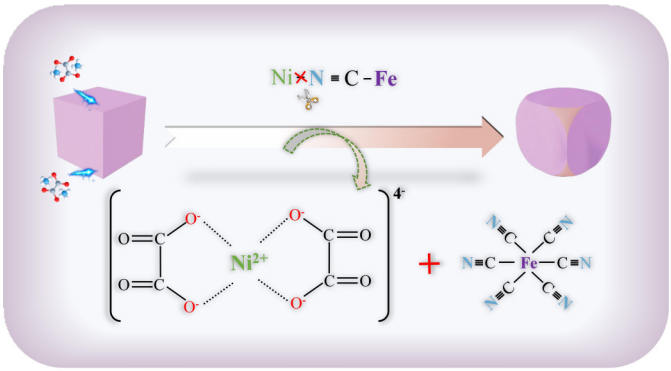

An ammonium oxalate etching strategy was employed to selectively transform nanocubes into octa-truncated cubes at elevated temperatures. By varying the amount of ammonium oxalate, the influence on the morphological evolution of the material was systematically investigated, and comprehensive electrochemical performance tests were conducted on the resulting materials.

Nano Research

Open Access

Research Article

From PBA nanocubes to octa-truncated cubes: The ammonium oxalate etching route for enhanced performance in aqueous Ni-Zn batteries

Yue Chen[1,2], Yichun Su[3,4], Mohsen Shakouri[5], Bin He[6], and Huan Pang [1]

[1] *School of Chemistry and Materials, Yangzhou University, Yangzhou 225002, China*
[2] *Interdisciplinary Research Center for Advanced Energy, Yangzhou University, Yangzhou 225127, China*
[3] *School of Chemistry and Chemical Engineering, Chongqing University of Science and Technology, Chongqing 401331, China*
[4] *School of Environmental Science, Nanjing Xiaozhuang University, Nanjing 211171, China*
[5] *Canadian Light Source Inc., University of Saskatchewan, Saskatoon S7N 2V3, Canada*
[6] *Zhejiang Key Laboratory for Industrial Solid Waste Thermal Hydrolysis Technology and Intelligent Equipment, Huzhou Key Laboratory of Environmental Functional Materials and Pollution Control, Department of Materials Engineering, Huzhou University, Huzhou 313000, China*

Received: 30 December 2026; **Revised:** 25 February 2026; **Accepted:** 25 March 2026

Address correspondence to huanpangchem@hotmail.com, panghuan@yzu.edu.cn

Cite this article: *Nano Research*, 2026, 19, 94908679 https://doi.org/10.26599/NR.2026.94908679

ABSTRACT: Prussian blue analogs (PBAs) are regarded as highly promising cathode materials for nickel-zinc batteries (NZBs) due to their simple preparation process and stable framework structure. However, their practical application remains limited by poor capacity retention and cycling stability. In this study, a chemical etching strategy using ammonium oxalate as the etchant was employed to transform nanocube structures into octahedrally truncated cubes. This defect engineering approach effectively enhanced the rate capability and cycling performance of the material. As a cathode material for NZBs, NiCoHCF-1.2 demonstrated an outstanding peak power density (31.83 mW cm^{-2}) and retained 63.29% of its capacity after 1000 cycles. This research provides a viable pathway for constructing novel nanostructured PBA materials and holds significant importance for advancing the development of advanced energy storage systems.

KEYWORDS: Prussian blue analog (PBA) nanocubes, etching, nickel-zinc battery, energy storage

1 Introduction

In the contemporary world, the global demand for efficient, safe and sustainable energy storage is experiencing explosive growth. As a core component of new energy storage devices, the development of battery technology is directly related to the future of the entire energy storage industry [1-5]. Aqueous nickel-zinc batteries (NZBs) demonstrate significant potential in the energy storage field due to their high safety, abundant reserves of nickel and zinc resources, and relatively low production costs. Furthermore, the battery system exhibits excellent specific capacity, high operating voltage and high energy density, making it an ideal choice for energy storage applications [6-8]. Currently, nickel-zinc batteries primarily use nickel oxide (NiO) [9-11], nickel hydroxide ($Ni(OH)_2$) [12-14], nickel molybdate ($NiMoO_4$) [15, 16], and some variants derived from the Ni^{2+}/Ni^{3+} redox reaction as cathode materials [17]. However, issues such as capacity decay and poor cycling stability of electrode materials remain major bottlenecks restricting their practical application [18]. The development of novel cathode materials is a critical breakthrough for advancing high-performance nickel-zinc batteries.

Prussian blue analogues (PBAs) are a typical class of coordination compounds characterized by a three-dimensional (3D) open framework structure, flexible and tunable composition, as well as simple preparation and low cost, making them a highly promising category of cathode materials for batteries [19-21]. The most common type of PBA utilizes $[Fe(CN)_6]$ as the ligand, and is consequently categorized as hexacyanoferrates (HCFs) [22]. It is worth noting that the inherent structural tunability and compositional customizability of PBAs facilitate their engineering into nanoscale dimensions (e.g., nanoparticles, nanocubes, or hollow nanostructures). These nanostructures serve a dual function: they provide a larger electrode-electrolyte contact area while shortening the diffusion pathways for ions/electrons, thereby synergistically enhancing capacity and cycling stability [23]. Etching is an effective method for modifying the structure of PBAs to construct nanomaterials [24-27]. Currently, the commonly used approaches involve acid or alkaline etching. For instance, Shi et al. developed a series of highly asymmetric PBA nanomaterials through the action of thiocyanuric acid (TCA). The concentration of TCA and the reaction temperature allow for precise control over the morphology and growth, enabling a shift in facet priority and demonstrating excellent control over instability [28]. In another study, Wang et al. subjected NiFe-PBA to in situ electrolysis by immersing it in a NaOH solution, yielding ultrathin NiFe-layered double hydroxide (LDH) nanosheets

rich in vacancies. The hierarchical architecture of NiFe-LDH@E-PBA offered advantages such as abundant active sites, large surface area, and rapid charge/mass transfer [29]. Compared with traditional acid-alkali etching, inorganic salt etching represents a superior green chemical strategy characterized by better controllability, milder conditions, and enhanced environmental friendliness. To date, reports on the use of inorganic salts as etching agents to treat PBAs for constructing nanostructured NiCoHCF remain relatively scarce [30].

In this study, NiCoHCF nanocubes were initially synthesized via a simple co-precipitation method. Subsequently, an ammonium oxalate etching strategy was employed to selectively transform NiCoHCF into octa-truncated cubes under elevated temperature. The morphology of NiCoHCF was modulated by varying the amount of ammonium oxalate (NiCoHCF-X, X=0, 0.1, 1.2, and 1.6 g), leading to optimized electrochemical performance of the electrode material. Additionally, the effects of reaction time and temperature on the morphological evolution, as well as the underlying structural transformation mechanism, were systematically investigated. Experimental results demonstrated that the truncated structure obtained after etching can effectively increase the electrode-electrolyte interfacial contact, shorten the electron transport pathways, and thereby enhance the electrical performance of the cathodes for NZBs. NiCoHCF-1.2//Zn@CC battery exhibited a remarkable areal capacity of 0.22 mAh cm^{-2} (at 3 mA cm^{-2}) and reached a peak power density as high as 31.83 mW cm^{-2}.

2 Results and Discussion

The synthetic route employed in this study is depicted in **Figure. 1**. Initially, the nano-cubic NiCoHCF was synthesized via a room-temperature co-precipitation method, using nickel chloride and cobalt chloride as metal sources and potassium ferricyanide as the ligand. Subsequently, the addition of ammonium oxalate at different concentrations was followed by a conversion into octa-deficient corner cubes using a water bath heating method. The as-synthesized samples presented

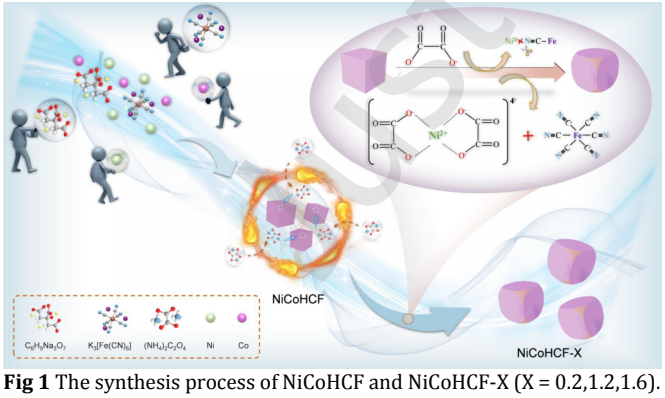

Fig 1 The synthesis process of NiCoHCF and NiCoHCF-X (X = 0.2,1.2,1.6).

a cubic morphology, which developed varying degrees of corner defects upon the amount of ammonium oxalate introduced. Site-selective etching at the corners of NiCoHCF by ammonium oxalate was initiated owing to the higher surface energy and richer defects [31]. In the coordination reaction, oxalate ions preferentially chelate with Ni and Co metal ions, thus diminishing the Ni-N≡C-Fe bonding and leading to the etched octa-truncated cubic structure [32].

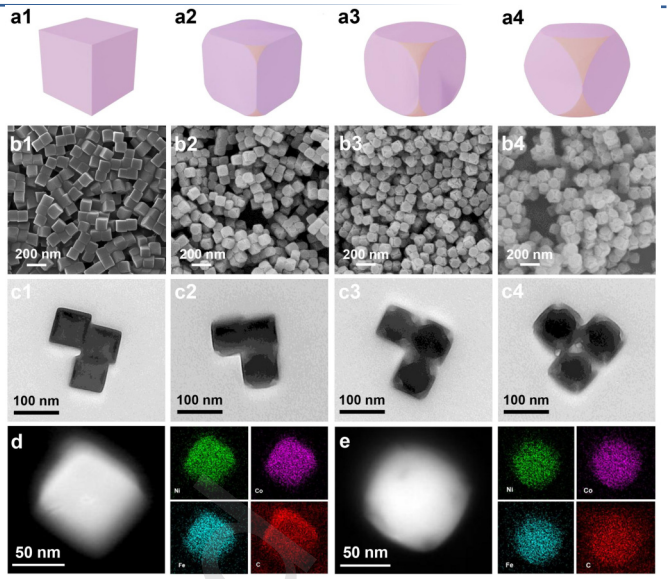

Fig 2 3D geometries (a), SEM images (b), TEM images (c) of NiCoHCF, NiCoHCF-0.2, NiCoHCF-1.2, NiCoHCF-1.6; HAADF-STEM image and corresponding elemental mapping images of (d) NiCoHCF and (e) NiCoHCF-1.2.

We illustrated the 3D morphological evolution of the material during etching, as shown in **Figure. 2a1-a4**. It can be clearly observed that the material initially exhibited a well-defined cubic structure with smooth surfaces and relatively few surface defects. As the amount of ammonium oxalate increased, more pronounced corner truncation developed on the cubic framework, which introduced additional surface defects. This structural modification is anticipated to enhance the functional properties of the material. Scanning electron microscopy (SEM) images reveal that the NiCoHCF exhibits a regular morphology with an average particle size of approximately 115 nm (**Figure. 2b1**). The cubic structure of NiCoHCF is also demonstrated by transmission electron microscopy (TEM) images (**Figure. 2c1**). With increasing concentrations of ammonium oxalate, the degree of etching at eight corners of the NiCoHCF cubes intensifies, resulting in progressively larger corner deficiencies (**Figure. 2b2-b4** and **Figure. 2c2-c4**). The etched NiCoHCF samples were designated as NiCoHCF-X (X = 0.2, 1.2, 1.6) based on the concentration of ammonium oxalate. Furthermore, etching reactions at other concentrations for the same duration (**Figures. S1**) and at different reaction times for the same concentration (**Figure. S2-S4**) were also investigated. To establish a clear structure-property relationship, three representative samples with well-defined morphological features were selected from the reacted NiCoHCF cubes for further investigation. To investigate the role of temperature, etching was also conducted at room temperature, as illustrated in **Figure. S5**. The cubic morphology showed no significant change, confirming that a high-temperature water bath is essential for achieving significant etching. Energy-dispersive spectrometer (EDS) mapping images of NiCoHCF and NiCoHCF-X (X = 0.2, 1.2, 1.6) confirm the homogeneous distribution of Ni, Co, Fe, and C elements (**Figure. 2d, e** and **Figure. S6**).

The structure of the materials was further characterized. As shown in **Figure. 3a**, the X-ray diffraction (XRD) patterns reveal that all materials exhibit similar crystalline phases. The characteristic peaks located at approximately 17.3°, 24.6°, 35.0°, and 39.3° can be indexed to (200), (220), (400),

and (420) lattice planes, respectively. The diffraction pattern shows good agreement with the theoretical simulation (PDF#51-1897), indicating that the structural integrity of the material is largely preserved throughout the etching treatment. Compared to NiCoHCF, the diffraction peaks of NiCoHCF-0.2, NiCoHCF-1.2, and NiCoHCF-1.6 are slightly shifted toward higher angles. According to the Bragg equation ($2d\sin\theta = n\lambda$), this indicates a reduction in interplanar spacing and an overall lattice contraction [33]. The XRD Rietveld refinement results in **Figure. S7** also support the above conclusion. The composition and structure of NiCoHCF and NiCoHCF-X were further confirmed by Fourier transform infrared spectroscopy (FTIR) and Raman spectroscopy. The peaks at 3406 and 1608 cm^{-1} are respectively identified as the the vibrational modes of water molecules (O-H stretching and bending). The absorption band from 2050 to 2170 cm^{-1} is characteristic of the C≡N stretching vibration in the PBA. The merging of the Fe^{3+}-CN and Fe^{2+}-CN peaks (at 2100 and 2160 cm^{-1}) into a broad band in the NiCoHCF-X samples suggests that the chelation of oxalate ions to nickel ions disrupts the original Ni-N≡C-Fe bonding. This spectral change suggests that the chelation of oxalate ions with nickel ions disrupts the Ni-N≡C-Fe coordination during the ligand substitution process. Under the influence of ammonium oxalate, the Fe^{2+}-CN framework was enhanced, gradually replacing the Fe^{3+}-CN species (**Figure. 3b**). As can be seen from **Figure. S8**, the C≡N sub-peak area ratio increases after etching, suggesting that the etching process exposes more C≡N groups. Raman spectroscopy also confirmed the successful synthesis, showing a characteristic peak at ≈2180 cm^{-1} corresponding to C≡N group in the PBA structure, thereby verifying the presence of $[Fe(CN)_6]^{4-}$ (**Figure. S9**) [34].

To investigate the changes in specific surface area and pore size of the material after etching, Brunauer-Emmett-Teller (BET) and Barrett-Joyner-Halenda (BJH) measurements were performed on NiCoHCF and NiCoHCF-1.2. The BET results, shown in **Figure. 3c** and **Figure. S10**, exhibit typical Type IV N_2 adsorption/desorption isotherms. The specific surface areas of NiCoHCF and NiCoHCF-1.2 are 174.07 and 45.16 $m^2 \cdot g^{-1}$, respectively. The reduction in specific surface area further indicates an increase in active sites of the etched NiCoHCF material [35]. Additionally, the average pore sizes of NiCoHCF and NiCoHCF-1.2 are 5.88 nm and 14.97 nm, respectively. The superior electrochemical performance of NiCoHCF-1.2 may be attributed to its favorable pore structure and pore size distribution. The etched NiCoHCF exhibits enhanced porosity and exposes more defects, which would be more conducive to charge transfer and ion diffusion [36]. The thermogravimetric analysis (TGA) results are shown in **Figure. S11**. The mass loss of the samples can be divided into three main stages: the mass loss in the first stage results from the removal of both adsorbed and crystalline water; the mass loss in the second stage (230-400 °C) is mainly associated with the partial decomposition of cyano groups in PBA; the third stage predominantly involves further decomposition of the PBA framework. The water contents in the NiCoHCF and NiCoHCF-1.2 samples are 22.29% and 16.52%, respectively, indicating a reduction in crystalline water after high-temperature etching, which contributes to performance improvement.

We employed X-ray photoelectron spectroscopy (XPS) to probe the surface chemical states and bonding characteristics of NiCoHCF and the etched NiCoHCF-1.2. The survey profiles in **Figure. 3d** reveal the coexistence of Ni, Co, Fe, N, and C elements on the surfaces of both materials. The observed peaks are assigned to their respective core levels as follows: 857 eV (Ni 2p), 783 eV (Co 2p), 708 eV (Fe 2p), 398 eV (N 1s), and 285 eV (C 1s). The high-resolution Ni 2p spectrum of NiCoHCF exhibits two peaks at binding energies of 859.49 eV and 876.07 eV, corresponding to Ni $2p_{3/2}$ and Ni $2p_{1/2}$, respectively (**Figure. 3e**). These main peaks indicate the coexistence of mixed-valence Ni species, specifically Ni^{3+} and Ni^{2+}. In NiCoHCF-1.2, the shift of the Ni $2p_{3/2}$ peak toward lower binding energy can be attributed to the etching process, which alters the local coordination environment and electronic structure of Ni. This enhances the electron cloud density around Ni atoms, leading to the observed decrease in binding energy. The high-resolution XPS spectra of Co 2p and Fe 2p (**Figure. 3f** and **S12b**) display peaks for Co $2p_{3/2}$, Co $2p_{1/2}$, Fe $2p_{3/2}$, and Fe $2p_{1/2}$. Each spectrum can be deconvoluted into two spin-orbit doublets, confirming the coexistence of Co^{2+}, Co^{3+}, Fe^{2+}, and Fe^{3+} within the metal-organic framework. From the N 1s and C 1s spectra (**Figure. S12a** and **S12c**), the main characteristic peaks are located at 398.2 eV and 286.0 eV, respectively, providing evidence for the presence of C≡N bonds [37]. Additionally, the specific peak positions and valence states of each element are summarized in **Table S1**.

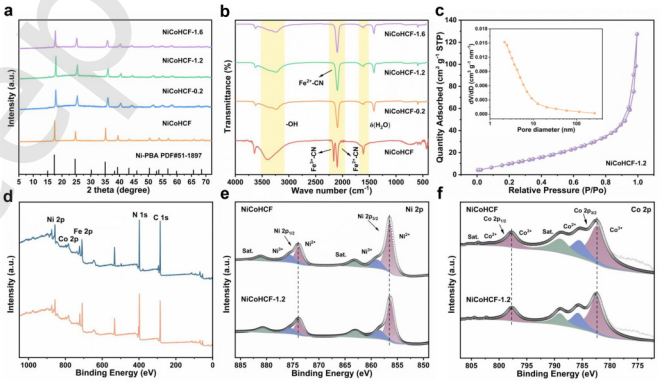

Fig 3 (a) XRD patterns (b) FTIR spectra of NiCoHCF, NiCoHCF-0.2, NiCoHCF-1.2 and NiCoHCF-1.6. (c) N_2 adsorption-desorption isotherms of NiCoHCF-1.2. (d) XPS survey spectra. (e) High-resolution Ni 2p XPS spectra. (f) High-resolution Co 2p XPS spectra.

To evaluate the electrochemical performance of NiCoHCF and NiCoHCF-X, the materials were loaded onto carbon cloth and initially assessed using a three-electrode system in 3 M KOH electrolyte. **Figure S13** displayed the XRD diffraction patterns of the bare carbon cloth substrate and NiCoHCF-X. As observed from the cyclic voltammetry (CV) curves in **Figure. S14**, both NiCoHCF and NiCoHCF-X exhibit similar shapes and well-defined redox peaks at scan rates ranging from 5 to 50 mV s^{-1}. At the scan rate of 5 mV s^{-1}, the redox peak area of NiCoHCF-X initially increases and then decreases with increasing ammonium oxalate concentration. Notably, NiCoHCF-1.2 demonstrates the largest redox peak area, indicating faster and more abundant redox reactions (**Figure. 4a**). Furthermore, the charge storage mechanism of the materials was studied using the power-law relationship between peak current (i) and scan rate (v), expressed as $i = av^b$. The b-values for the anodic/cathodic peaks of both NiCoHCF and NiCoHCF-X electrodes are close to 0.5, suggesting a diffusion-controlled process (**Figure. S15**).

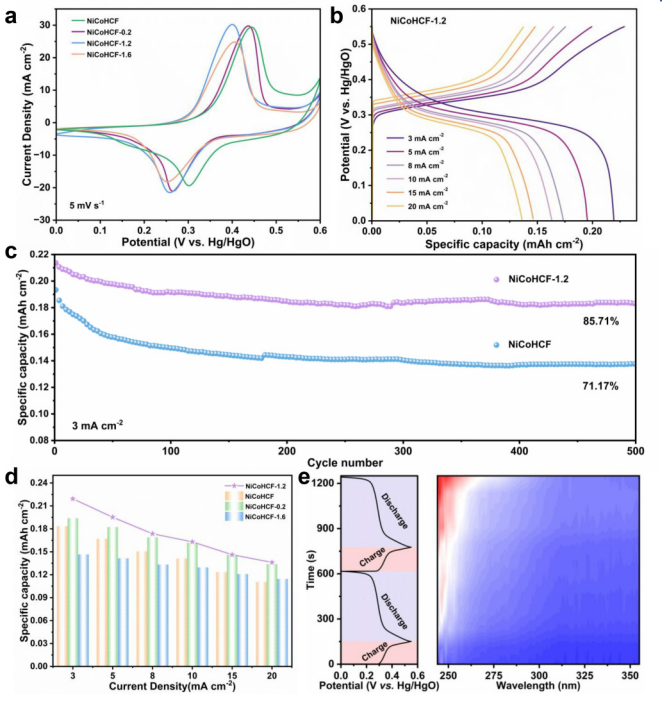

Fig 4 (a) CV curves of NiCoHCF and NiCoHCF-X at 5 mV/s. (b) GCD profiles of NiCoHCF-1.2 from 3 to 20 mA/cm^2. (c) Cycling performance of NiCoHCF and NiCoHCF-1.2 over 500 GCD cycles. (d) Specific capacitance of the obtained electrodes at increasing current densities. (e) In situ UV-vis spectra of NiCoHCF-1.2 during charge-discharge cycling.

We further employed galvanostatic charge-discharge (GCD) curves to investigate how ammonium oxalate etching affects the specific capacity. **Figure 4b** and **Figure S16** display the GCD curves of NiCoHCF and NiCoHCF-X electrodes at different current densities spanning a range from 3 to 20 mA cm^{-2}. Notably, the NiCoHCF-1.2 electrode exhibited a superior discharge plateau and the highest areal specific capacity (0.22 mAh cm^{-2}) at 3 mA cm^{-2} (**Figure. S17**). Therefore, the defects introduced by etching contribute to enhanced specific capacity. However, excessive etching (as in NiCoHCF-1.6) results in a lower voltage plateau compared to NiCoHCF-1.2, which adversely affects the Ni redox reactions during charge/discharge processes. As shown in **Figure. 4d**, NiCoHCF-1.2 delivered the highest specific capacity across all current densities, demonstrating superior rate performance. Electrochemical impedance spectroscopy (EIS) measurements of NiCoHCF and NiCoHCF-X electrodes (**Figure. S18**) reveal that the semicircle in the Nyquist plot corresponds to the charge transfer resistance (Rct). The smaller Rct value observed for NiCoHCF-1.2 indicates faster charge transfer kinetics, likely attributable to the enlarged pore diameter after etching that facilitates charge transport. Furthermore, the areal power/energy density of NiCoHCF and NiCoHCF-X under identical testing conditions are compared in **Figure. S19**. NiCoHCF-1.2 exhibits optimal areal energy density and power density (0.068 mWh cm^{-2} and 5.44 mW cm^{-2}) among the electrode materials. The cycling stability of pristine NiCoHCF and etched NiCoHCF-1.2 electrodes after 500 cycles is presented in **Figure. 4c**. The results show that the etched NiCoHCF-1.2 maintains a capacity retention of 85.71%, significantly higher than the 71.17% retention of the pristine material.

To further investigate the energy-storage mechanism of the NiCoHCF-1.2 cathode, in situ UV-Vis test was conducted in a three-electrode system during charge-discharge cycling (**Figure. 4e**). The obtained spectra exhibited a characteristic absorption band around 250 nm, which is assigned to ligand-to-metal charge transfer. As cycling progressed, the onset of this absorption exhibited a slight red-shift, implying electronic coupling between the metal center and the ligand [38]. During the second cycle, the absorption intensity of this band increased, suggesting potential dissolution of ligands from NiCoHCF-1.2 during the charge-discharge process.

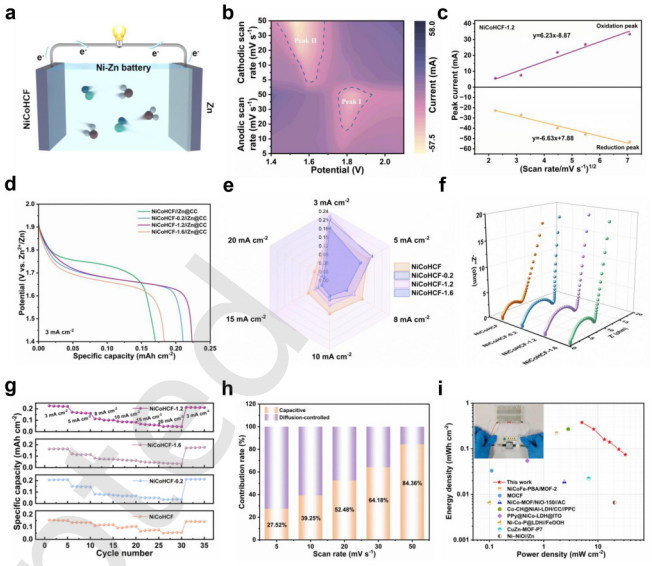

Fig 5 (a) Schematic illustration of the aqueous NZBs battery. (b) Contour plots of CV pattern for NiCoHCF-1.2 electrode. (c) Fitting plots between peak current and (scan rate)$^{1/2}$. (d) GCD curves of four NZBs at 3 mA/cm^2. (e) Specific capacitance of NiCoHCF and NiCoHCF-X (X = 0.2,1.2,1.6) under various current densities. (f) Comparative EIS spectra in Nyquist plots. (g) Rate performances of NiCoHCF and NiCoHCF-X (X = 0.2,1.2,1.6). (h) The contribution ratios of the NiCoHCF-1.2 electrode. (i) Ragone plots of the aqueous NiCoHCF-1.2 //Zn compared with other works.

To evaluate the electrochemical performance of NiCoHCF and NiCoHCF-X electrodes as cathode materials for aqueous Zn-based batteries (NZBs), we constructed NiCoHCF//Zn@CC and NiCoHCF-X//Zn@CC aqueous batteries using a 3 M KOH and 20 mM $Zn(Ac)_2$ mixed solution as the electrolyte for two-electrode electrochemical testing (**Figure. 5a**). The CV responses of the NiCoHCF//Zn@CC and NiCoHCF-X//Zn@CC within the operating window of 1.4-2.1 V are depicted in **Figure. 5b** and **Figure. S20**. All materials exhibit well-defined CV curves with typical battery characteristics at various scan rates. The NiCoHCF-1.2//Zn@CC cell demonstrates more distinct redox peaks and a larger CV area at 5 mV s^{-1}, suggesting a higher charge storage capacity (**Figure. S21**). As shown in **Figure. 5c**, the peak redox current density (i) of the NiCoHCF-1.2//Zn@CC cell was plotted against the square root of the scan rate ($v^{1/2}$). The resulting linear relationship indicates a high b-value, implying a diffusion-controlled process with rapid ion diffusion kinetics. The GCD curves of NiCoHCF//Zn@CC and NiCoHCF-X//Zn@CC at current densities ranging from 3 to 20 mA cm^{-2} exhibit discharge plateaus above 1.7 V (**Figure. S22**), confirming stable voltage output for all materials. When tested at 3 mA cm^{-2}, the areal capacities of NiCoHCF//Zn@CC, NiCoHCF-0.2//Zn@CC, NiCoHCF-1.2//Zn@CC, and NiCoHCF-1.6//Zn@CC are 0.170, 0.210, 0.223, and 0.183 mAh cm^{-2}, respectively. The NiCoHCF-1.2//Zn@CC configuration delivers the highest specific capacity along with a higher discharge plateau, suggesting faster reaction kinetics (**Figure. 5d**). Similarly, as clearly observed in **Figure. 5e**,

NiCoHCF-1.2//Zn@CC demonstrates superior areal capacity compared to other materials across various current densities. Compared to the conventional mass loading used in experiments, electrochemical data were collected for electrodes with a mass loading of ≥10 mg cm^{-2} (**Figure. S23**). The areal capacity of the thick electrode reached 0.48 mAh cm^{-2}, demonstrating the excellent scalability of the material. EIS measurements of all materials in the two-electrode system are presented in **Figure. 5f**. **Figure S24** displays the EIS fitting spectra for NiCoHCF-1.2 and its corresponding equivalent circuit, revealing a charge transfer resistance (Rct) of 9.14 Ω. The lower Rct value compared to other electrode materials indicates faster charge transfer kinetics. Furthermore, both NiCoHCF//Zn@CC and NiCoHCF-X//Zn@CC exhibit good rate capability. As shown in **Figure. 5g**, NiCoHCF-1.2//Zn@CC achieves an average specific capacity of approximately 0.223 mAh cm^{-2} at 3 mA cm^{-2}. When the current density is returned to 3 mA cm^{-2} after 30 cycles at varying rates, the average specific capacity recovers to 0.212 mAh cm^{-2}, demonstrating high capacity and electrochemical reversibility. The scan-rate dependence of the capacitive fraction for the NiCoHCF-1.2//Zn@CC electrode is displayed in **Figure. 5h**. Evidently, the capacitive contribution increases with increasing scan rate. At scan rates below 20 mV s^{-1}, the charge storage is primarily dominated by diffusion-controlled processes. In contrast, at higher scan rates above 20 mV s^{-1}, capacitive behavior contributes more significantly. A dominant capacitive contribution of 84.36% is achieved at 20 mV s^{-1}, indicating superior electrochemical performance.

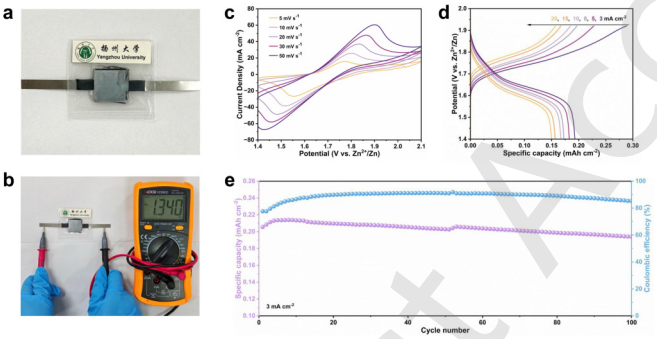

Fig 6 (a) Schematic diagram of the assembled device. (b) Voltage stability of gel batteries. (c) CV curves at varying scan rates. (d) GCD profiles under different current densities. (e) Charge-discharge cycling test.

In addition, **Figure 5i** compares the areal energy and power densities of the NiCoHCF-1.2//Zn battery with those reported in other relevant aqueous battery systems. The Ragone plot analysis demonstrates the superior performance of the NiCoHCF-1.2//Zn battery, reaching peak power and energy densities of 31.83 mW cm^{-2} and 0.37 mWh cm^{-2}, outperforming other reported works (**Table S2**). Furthermore, the cycling performance of NiCoHCF//Zn@CC and NiCoHCF-1.2//Zn@CC cells at 3 mA cm^{-2} is shown in **Figure. S25**. After 1000 cycles, the NiCoHCF-1.2 electrode maintains a capacity retention of 63.29%, demonstrating exceptional cycling stability (**Table S3**). SEM images in **Figure. S26** confirm that the material remains firmly adhered to the surface without detachment after cycling.

Based on the excellent electrochemical performance of the NiCoHCF-1.2//Zn aqueous battery, we fabricated a gel battery to explore its potential for practical applications. The flexible NiCoHCF-1.2//Zn@CC device was assembled by using NiCoHCF-1.2@CC as the cathode, polyacrylic acid gel as the solid-state electrolyte, and a zinc sheet as the anode, all encapsulated with a laminated film (**Figure. 6a-b**). The gel battery exhibited an open-circuit voltage of 1.340 V. The assembled device was used to power small electronic components, successfully lighting three LED bulbs. Subsequent electrochemical characterization revealed that the gel battery maintained 94.31% capacity retention after 100 cycles at a current density of 5 mA cm^{-2}, demonstrating exceptional cycling stability (**Figure. 6c-e**). These results confirm the remarkable electrochemical performance of the device and its feasibility for flexible energy storage applications. The enhanced charge transport capability of the salt-etched NiCoHCF-1.2 material offers valuable insights for the next generation of flexible energy storage devices, informing the design of safer, more scalable, and high-potential flexible power sources.

3 Conclusion

In this work, we investigated an ammonium oxalate etching strategy for the conversion of NiCoHCF nanocubes into truncated octahedral structures and their application in aqueous nickel-zinc batteries. The amount of ammonium oxalate introduced was found to significantly influence the morphological evolution of the NiCoHCF nanocubes. During the coordination process, the incorporation of ammonium oxalate exposed more metal ions, and the etched NiCoHCF-1.2 with optimal defect density exhibited enhanced specific capacity and improved electrochemical stability. This study successfully demonstrated that inorganic salts can effectively etch PBAs to construct nanostructured materials with tailored morphologies. These findings underscored the potential of such engineered nanomaterials to position PBAs as promising candidates for high-performance electrochemical energy storage devices.

Electronic Supplementary Material: Supplementary material (Electrochemical Measurements, XRD, XPS) is available in the online version of this article at https://doi.org/10.26599/NR.2026.94908679.

Data availability

All data needed to support the conclusions in the paper are presented in the manuscript and/or the Electronic Supplementary Material. Additional data related to this paper may be requested from the corresponding author upon request.

Acknowledgements

This work was supported by the National Natural Science Foundation of China (52371240), the Key Basic Research Program of Jiangsu Province (BK20253046), and Yangzhou Innovation Capability Enhancement Fund/program (SCX2025020017).

Declaration of competing interest

All the contributing author(s) report(s) no conflict of interests in this work.

Author contribution statement

Y. C.: Writing – original draft, formal analysis, data curation, conceptualization. Y. C. S.: Visualization, validation. M. S.: Data curation, conceptualization. B. H.: Project administration. H. P.: Supervision, resources, conceptualization. All the authors have approved the final manuscript.

Informed consent
Not applicable.

Ethics statement
Not applicable.

Use of AI statement
None.

References

[1] Wu, N.; He, W.; Shi, S.; Yuan, X.; Li, J.; Cao, J.; Yuan, C.; Liu, X. Bamboo fiber-derived carbon support for the immobilization of Pt nanoparticles to enhance hydrogen evolution reaction. *J. Colloid Interface Sci.* **2025,** *684*, 658-667.

[2] Cao, W.; Zhu, J.; Ni, J.; Li, L. Challenges and perspectives in aqueous zinc-nickel batteries. *Mater. Today Energy* **2025,** *51*, 101892.

[3] Wu, N.; Zhao, Z.; Zhang, Y.; Hua, R.; Li, J.; Liu, G.; Guo, D.; Zhao, J.; Cao, A.; Sun, G.; Hou, H.; Liu, X. Revealing the fast reaction kinetics and interfacial behaviors of $CuFeS_2$ hollow nanorods for durable and high-rate sodium storage. *J. Colloid Interface Sci.* **2025,** *679*, 990-1000.

[4] Zhao, D.; Qin, J.; Zheng, L.; Guo, D.; Wang, J.; Cao, M. Covalent interfacial coupling of vanadium nitride with nitrogen-rich carbon textile boosting its lithium storage performance as binder-free anode. *Nano Res.* **2021**, *14*, 4336-4346.

[5] Guo, D.; Qin, J.; Yin, Z.; Bai, J.; Sun, Y. K.; Cao, M. Achieving high mass loading of $Na_3V_2(PO_4)_3$@carbon on carbon cloth by constructing three-dimensional network between carbon fibers for ultralong cycle-life and ultrahigh rate sodium-ion batteries. *Nano Energy* **2018**, *45*, 136-147.

[6] Zheng, L.; Yi, F.; Liang, J.; Lu, M.; Kong, J.; Gao, A.; Shu, D. Construction of low-crystallinity three-dimensional flower-like cobalt-doped nickel hydroxide for high-performance nickel-zinc batteries. *ACS Appl. Mater. Interfaces* **2025,** *17*, 7793-7803.

[7] Zheng, L.; Yi, F.; Kong, J.; Meng, T.; Shu, D.; Gao, A.; Liang, J.; Lu, M. Highly loaded self-supported hollow urchin-like metallic organic framework for high-performance nickel-zinc batteries. *J. Power Sources* **2025,** *631*, 236309.

[8] Su, Y.; Zhang, Y.; Feng, W.; Zhang, G.; Sun, Y.; Yin, C.; Yuan, G.; Tang, Y.; Zhou, W.; Chen, H. C.; Pang, H. Monocarboxylic acid structural analogues facilitate in situ composite of functional complexes for aqueous batteries. *Angew. Chem. Int. Ed.* **2025,** *64*, 2752.

[9] Liang, N. N.; Qiu, Z.; Kim, D. J.; Han, D. S.; Kim, T. W.; Park, H. Active NiO outperforms other Ni-based catalysts for urea electrolysis. *J. Environ. Chem. Eng.* **2025,** *13*, 117830.

[10] Gemachu, L. Y.; Terefa, F. H.; Berhanu, A. L.; Bogale, R. F. Comparison of sunlight-driven photocatalytic activity of eco-friendly synthesized ZnO/CuO, ZnO/NiO and NiO/CuO binary nanocomposites. *Results Chem.* **2025,** *18*, 102708.

[11] Marnadu, R.; Mohan, K. S.; Farahim, F.; Shkir, M.; Minnam Reddy, V. R.; Arunkumar, S.; Packiaraj, R. Incorporation of Co ions on the physical properties of NiO nanoparticles and fabrication of superior photo-response p-Co-doped NiO/n-Si heterostructure-based diodes. *J. Phys. Chem. Solids* **2025,** *205*, 112793.

[12] He, Z. D.; Tesch, R.; Eslamibidgoli, M. J.; Eikerling, M. H.; Kowalski, P. M. Low-spin state of Fe in Fe-doped NiOOH electrocatalysts. *Nat. Commun.* **2023,** *14*, 3498.

[13] Wang, S.; Su, Y.; Jiang, Z.; Meng, Z.; Wang, T.; Yang, M.; Zhao, W.; Chen, H.; Shakouri, M.; Pang, H. Metal-hydroxide organic frameworks for aqueous nickel-zinc batteries. *Nano Lett.* **2024,** *24*, 15101-15109.

[14] Xu, K.; Zhang, S.; Hu, Y.; Zhuang, X.; Zhang, G.; Du, M.; Gong, H.; Zheng, M.; Pang, H. Self-assembly of 1D-2D NiCoAl-LDH nanostructures with cationic vacancy defects for electrochemical energy storage. *J. Energy Storage* **2025,** *108*, 115040.

[15] Ma, M.; Tan, J. L.; Liu, H. Z.; Qi, Y.; Wen, X.; Zhang, C.; Ouyang, D.; Chai, Y. M.; Dong, B. Electronic structure modulation in $Ni(OH)_2$ /$NiMoO_4$ n-n heterojunctions for enhanced alkaline hydrogen evolution. *J. Electroanal. Chem.* **2025,** *996*, 119430.

[16] Kannan, V.; Kim, H. J.; Park, H. C.; Kim, H. S. Single-step direct hydrothermal growth of $NiMoO_4$ nanostructured thin film on stainless steel for supercapacitor electrodes. *Nanomaterials* **2018,** *8*, 563.

[17] Zhang, X.; Noréus, D. Selenized Zn-doped $NiMoO_4$ modified with the prussian blue analogue as electrodes for aqueous alkaline NiZn batteries. *Chem. Eng. J.* **2025,** *519*, 165666.

[18] Cui, B.; Chen, Y.; Xu, H.; Feng, W.; Su, Y.; Zhang, Y.; Liu, Z.; Zhou, H.; Pang, H. Bimetallic synergy and interlayer π-π modulation in nickel-cobalt metal-organic frameworks enhancement of the performance of nickel-zinc batteries. *Sci. China Chem.* **2026**, *69*, 174-181.

[19] Wang, X.; Zhao, M.; Du, W.; Zhang, C.; Li, W.; Yang, C.; Liu, Y. Boosting ultralong lifespan of Fe-based prussian blue analogs cathode via element doping and crystal water capture. *Chem. Eng. J.* **2025,** *508*, 160997.

[20] Feng, W.; Li, B.; Yuan, G.; Li, Y.; Zhang, Y.; Du, M.; Su, Y.; Tang, Y.; Yue, H.; Li, Y.; Shakouri, M.; Chen, H. C.; Li, W.; Liu, Z.; Pang, H. High performance aluminum ion batteries enabled by the coordination between vanadium‐based PBAs cathode and aqueous eutectic electrolyte. *Adv. Sci.* **2025**, *12*, e11274.

[21] Tan, Y.; Chen, D.; Kotsiubynskyi, V.; Li, G.; Shen, L.; Han, W. Prussian blue and its analogues nanomaterials: A focused view on physicochemical properties and precise synthesis. *J. Energy Chem.* **2025,** *107*, 393-406.

[22] Xiao, M. Research progress of prussian blue analogues for cathode of sodium ion batteries. *J. Alloys Compd.* **2025,** *1036*, 182014.

[23] Ye, J.; Zhuang, G.; Wen, Y.; Wei, J.; Chen, J.; Zhuang, Z.; Yu, Y. Three-dimensional zigzag Prussian blue analogue and its derivates for bisphenol a scavenging: Inhomogeneous spatial distribution of Fe^{III} in anisotropic etching of PBA. *Chem. Eng. J.* **2019,** *372*, 260-268.

[24] Zhao, Y.; Peng, J.; Chen, K.; Luo, L.; Chen, H.; Zhang, H.; Chou, S.; Feng, X.; Chen, W.; Cao, R.; Ai, X.; Fang, Y.; Cao, Y. Boosting the sodium storage performance of prussian blue analogues via effective etching. *Sci. China Chem.* **2023,** *66*, 3154-3160.

[25] Gao, J.; Hao, Y.; Lin, S.; Zhang, Z.; Li, H.; He, Y. Etching and isolation technique for synthesis of CNTs-encapsulated $NiSe_2$/$CoSe_2$ for supercapacitor applications. *Chem. Eng. J.* **2025,** *504*, 158572.

[26] Zhang, H.; Diao, J.; Ouyang, M.; Yadegari, H.; Mao, M.; Wang, M.; Henkelman, G.; Xie, F.; Riley, D. J. Heterostructured core-hell Ni-Co@Fe-Co nanoboxes of prussian blue analogues for efficient electrocatalytic hydrogen evolution from alkaline seawater. *ACS Catal.* **2023,** *13*, 1349-1358.

[27] Shi, C.; Ye, S.; Wang, X.; Meng, F.; Liu, J.; Yang, T.; Zhang, W.; Wei, J.; Ta, N.; Lu, G. Q.; Hu, M.; Liu, J. Modular construction of prussian blue analog and TiO_2 dual-compartment janus nanoreactor for efficient photocatalytic water splitting. *Adv. Sci.* **2021,** *8*, 2001987.

[28] Shi, J.; Yang, Z. X.; Nie, J.; Huang, T.; Huang, G. F.; Huang, W. Q. Regioselective super-assembly of prussian blue analogue. *J. Colloid Interface Sci.* **2024,** *667*, 44-53.

[29] Wang, C.; Chen, L.; Xu, X.; Liu, Y.; Song, Y.; Zong, L.; Li, X.; Chen, G.; Zhan, T. Vacancies-riched composite of ultrathin NiFe-LDH nanosheets on the etched prussian blue analogue: An efficient alkaline oxygen evolution electrocatalyst. *Int. J. Hydrogen Energy* **2025,** *98*, 783-792.

[30] He, Y.; Xiao, Y.; Ma, X.; Guo, K.; Guo, L.; Fan, A.; Zheng, X.; Ai, F.; Yan, X. Sensitive chemiluminescence detection platform for H_2O_2 and glucose through facile inorganic salt etching of cobalt prussian blue analogues. *Microchim. Acta* **2025,** *192*, 411.

[31] Yin, J.; Wang, C.; Zhang, K.; Liu, D.; Wu, Z.; Hata, S.; Yu, R.; Shiraishi, Y.; Du, Y. Heterostructure engineering and ultralow Pt-loaded multicomponent nanocage for efficient electrocatalytic oxygen evolution. *J. Colloid Interface Sci.* **2023,** *639*, 214-222.

[32] Cui, X.; Ma, F.; Lei, G.; Jiang, W.; Yang, X.; Liu, Z.; Wan, J.; Liu, Y. Trisodium citrate as a double‐edged sword: Selective etching prussian blue analog nanocubes into orthogonal frustums and their derivatives for supercapacitors. *Small* **2024,** *20*, 2403732.

[33] Du, C. Y.; Luo, R. J.; Li, X. L.; Wu, K.; Liu, N.; Ma, C.; Bao, J.; Zeng, J.; Xu, X.; Zhou, Z. T.; Zhou, Y. N. Coupling active and inactive transition metals to boost calcium storage cycle stability for prussian blue cathodes. *J. Colloid Interface Sci.* **2025,** *683*, 543-551.

[34] Cao, J.; Xue, Y.; Ji, Z.; Pu, J.; Shen, X.; Kong, L.; Yuan, A. CoNi hexacyanoferrate nanoparticles anchored on carbon nanotubes as superior cathode materials for rechargeable aqueous zinc-ion batteries. *J. Energy Storage* **2024,** *86*, 111413.

[35] Chen, T.; Wang, F.; Cao, S.; Bai, Y.; Zheng, S.; Li, W.; Zhang, S.; Hu, S. X.; Pang, H. In situ synthesis of MOF-74 family for high areal energy density of aqueous nickel-zinc batteries. *Adv. Mater.* **2022,** *34*, 2201779.

[36] Tauseef, A.H.; Adeel, A. M.; Nisar, T.; Wagner, V.; Adil, M. M.; Haider, A.; Ali, S. Electrochemical synthesis of Co-, Ni- and NiCo-based hexacyanocobaltates as efficient electrocatalysts for water oxidation studies. *Inorg. Chem. Commun.* **2023**, *154*, 110916.

[37] Wang, J.; Yang, A.; Li, J.; Su, K.; Tang, Y.; Qiu, X. Top-down and facet-selective phase-segregation to construct concave nanocages with strongly coupled hetero-interface for oxygen evolution reaction. *Appl. Catal., B* **2022,** *300*, 120727.

[38] Wang, Z.; Henke, S.; Paulus, M.; Welle, A.; Fan, Z.; Rodewald, K.; Rieger, B.; Fischer, R. A. Defect creation in surface-mounted metal-organic framework thin films. *ACS Appl. Mater. Interfaces* **2019,** *12*,

2655-2661.

Electronic Supplementary Material

From PBA nanocubes to octa-truncated cubes: The ammonium oxalate etching route for enhanced performance in aqueous Ni-Zn batteries

Yue Chen[1,2], Yichun Su[3,4], Mohsen Shakouri[5], Bin He[6], and Huan Pang [1]

[1] *School of Chemistry and Materials, Yangzhou University, Yangzhou 225002, China*
[2] *Interdisciplinary Research Center for Advanced Energy, Yangzhou University, Yangzhou 225127, China*
[3] *School of Chemistry and Chemical Engineering, Chongqing University of Science and Technology, Chongqing 401331, China*
[4] *School of Environmental Science, Nanjing Xiaozhuang University, Nanjing 211171, China*
[5] *Canadian Light Source Inc., University of Saskatchewan, Saskatoon S7N 2V3, Canada*
[6] *Zhejiang Key Laboratory for Industrial Solid Waste Thermal Hydrolysis Technology and Intelligent Equipment, Huzhou Key Laboratory of Environmental Functional Materials and Pollution Control, Department of Materials Engineering, Huzhou University, Huzhou 313000, China*

Address correspondence to huanpangchem@hotmail.com, panghuan@yzu.edu.cn

Supporting information to https://doi.org/10.26599/NR.2026.94908679

Experimental section

All reagents were of analytical grade and could be used without further purification. Nickel chloride hexahydrate ($NiCl_2·6H_2O$, 99.5%), Cobalt chloride hexahydrate ($CoCl_2·6H_2O$, 99.5%), potassium hexacyanoferrate(III) ($K_3[Fe(CN)_6]$), and Ammonium oxalate monohydrate ($C_2H_8N_2O_4·H_2O$, 99%) were purchased from Shanghai Sinopharm Chemical Reagent. Trisodium citrate dihydrate ($C_6H_5Na_3O_7·2H_2O$) was purchased from Macklin. Potassium hydroxide (KOH, 95%), Zinc acetate dihydrate ($C_4H_{10}O_6Zn·2H_2O$, 99%) were purchased from Aladdin. All aqueous solutions were prepared with high-purity de-ionized water (DI water, resistance 18 MΩ cm^{-1}). Polyacrylic acid-based gel electrolytewas purchased from Shanghai Yanwen Technology Co. Ltd.

Instrument required for experiment

Electronic analytical balance (FA-1004B), purchased from Shanghai Youke Instrument Co., Ltd. The phase and crystal structure of the material were characterized by X-ray diffraction (XRD) on a Bruker D8 Advanced X-ray Diffractometer (Cu-Kα radiation: λ = 0.15406 nm). The morphology of samples was observed by scanning electron microscope (SEM, Zeiss_Supra55) under the acceleration voltage of 5.0 kV. Transmission electron microscopy (TEM) investigations were performed by a JEM-2100 instrument. Energy dispersive X-ray spectrometry (EDS) elemental mapping scans were recorded using Tecnai G2 F30 S-TWIN at an acceleration voltage of 300 kV. The chemical states were measured using an Axis Ultra X-ray photoelectron spectroscope (XPS, Thermo Fisher Scientific ESCALAB250Xi) equipped with a standard monochromatic Al-Kα source (hv = 1486.6 eV). Fourier transform infrared (FTIR) transmission spectra were obtained on a BRUKER-EQUINOX-55 IR spectrophotometer. N_2 adsorption desorption isotherms were obtained on Quantachrome Instruments, Autosorb IQ3. The products were tested by Raman on a DXRxi Raman Imaging Microscope for functional group analysis. Additionally, thermogravimetry analysis (TGA) was performed by a PerkinElmer Pyris 1 TGA instrument under N_2 atmosphere from 20 °C to 800 °C at a heating rate of 10 °C min^{-1}. Electrochemical workstation (CHI-660E), purchased from CH Instruments, USA.

Materials synthesis

Synthesis of NiCoHCF:

In a typical procedure, 2.4 mmol of $NiCl_2·6H_2O$, 0.6 mmol of $CoCl_2·6H_2O$, 4.5 mmol of $Na_3C_6H_5O_7·2H_2O$ were dissolved in 100 mL of deionized water to obtain solution A. Then 2 mmol of $K_3[Fe(CN)_6]$ was dissolved in 100 mL of deionized water to obtain solution B. Then the solution B was poured directly into the solution A with stirring at room temperature. After 10 min of continuous stirring, the resulting mixed solution was aged for 24 h at room temperature. The products were collected by centrifugation and washed repeatedly with deionized water and ethanol, respectively.

Synthesis of NiCoHCF-X (X=0.2, 1.2, 1.6):

In a typical procedure, 0.1 g of NiCoHCF was dissolved in 20 mL of ethanol to obtain solution A. 0.2 g of ammonium oxalate monohydrate was dissolved in 80 mL of deionized water to obtain solution B. Then the solution B was poured directly into the solution A with stirring at room temperature. After continuous stirring for 10 minutes, the mixture was reacted at 90 °C for 1 hours to obtain NiCoHCF-0.2. The products were collected by centrifugation and washed repeatedly with deionized water and

ethanol, respectively. The NiCoHCF-1.2 and NiCoHCF-1.6 were prepared in the same way as above, except changing the amount of ammonium oxalate monohydrate to 1.2 and 1.6 g, respectively.

Preparation of NiCoHCF and NiCoHCF-X (X=0.2, 1.2, 1.6) electrodes

Prior to the preparation, the carbon cloth (CC) was first ultrasonically cleaned in acetone, absolute ethanol and DI water alternately for 3-4 times for 30 min each time. Then, the treated CC was placed in a vacuum drying oven to be dried at 60 °C overnight. To fabricate the working electrodes, active materials, acetylene black, and polyvinylidene difluoride (PVDF) were well mixed in a weight ratio of 8:1:1 in N-methyl pyrrolidone (NMP). Then, the formed slurry was sonicated for 30 min before depositing on a 1 cm × 2 cm CC, ensuring samples coated within 1 cm × 1 cm. The typical mass loading of the active material was about 2.4 mg cm^{-2}. Finally, NiCoHCF and NiCoHCF-X (X=0.2, 1.2, 1.6) electrodes were acquired after drying overnight at 60 °C in a vacuum drying oven.

Electrochemical measurements

Electrochemical measurements of NiCoHCF and NiCoHCF-X (X=0.2, 1.2, 1.6) (1 x 1 cm^2) were carried out in a three- electrode system in an aqueous electrolyte of KOH (3 M) using an electrochemical workstation (CHI 660E). The alternating current frequency ranged from 0.01 to 105 Hz with an amplitude of 5 mV. Open circuit potential was read and used. A Pt wire was used as the counter electrode and a Hg/HgO electrode was the reference electrode. Electrochemical measurements of nickel-zinc batteries were performed in a two-electrode system with 3 M KOH + 20 mM zinc acetate ($Zn(Ac)_2$) as the electrolyte. The NiCoHCF and NiCoHCF-X (X=0.2, 1.2, 1.6) (1 x 2 cm^2) were the cathode and Zn (1 x 2 cm^2) was the anode. The used area of electrode was 1 cm^2. 10 cycles of electrochemical activation process were carried out before electrochemical testing. The areal energy density and power density was calculated based on the area deposited with the sample (1 cm × 1 cm).

Calculations

The areal specific capacity C_A (mA h cm^{-2}) of the working electrodes in three-electrode system were calculated from discharge curves according the following equation:

$$C_A = \frac{I \times \Delta t}{S} \qquad (1)$$

where I (mA) is the discharging current, Δt (h) is the discharging time, and S (cm^2) is the area of the electrodes (1 cm^2).

Alternatively, the areal specific capacity of the NZBs (Cell) in two-electrode system was calculated from the discharging curves according the following equation:

$$C_{cell} = \frac{I \times \Delta t}{S} \qquad (2)$$

where C_{cell} (mA h cm^{-2}) is the areal specific capacity of the NZBs, I (mA) is the discharging current, Δt (h) is the discharging time, and S (cm^2) is the total surface area of the NZBs (1 cm^2).

The areal energy density (E) and areal power density (P) of the battery were calculated from the following equations:

$$\mathrm{E} = \frac{I \int_0^{\Delta t} U(t)\, dt}{S} \qquad (3)$$

$$\mathrm{P} = \frac{E}{\Delta t} \qquad (4)$$

where E (mW h cm^{-2}) is the areal energy density, I (mA) is the discharge current, $U(t)$ is the voltage during discharge (V), dt is the time differential, Δt (h) is the discharging time, and S (cm^2) is the total surface area of the NZBs (1 cm^2). P (mW cm^{-2}) is the areal power density and Δt (h) is the discharging time.

The kinetic of capacitive contribution can be obtained through calculating the CV curves at different scan rates. The relationship between current (i) and scan rate (v) can be written as:

$$i = av^b \qquad (5)$$

$$\log(i) = \log(a) + b\log(v) \qquad (6)$$

where a and b are constant can be obtained from $\log(v)$ versus $\log(i)$ plots. When b = 0.5 represents an ideal diffusion-controlled process and when b = 1.0 indicates a surface capacitive-controlled process.

Furthermore, the ratio of capacitive contribution could be described as the following equation:

$$i = k_1 v + k_2 v^{1/2} \qquad (7)$$

where $k_1 v$ and $k_2 v^{1/2}$ correspond to capacitive and diffusion contribution, respectively [1].

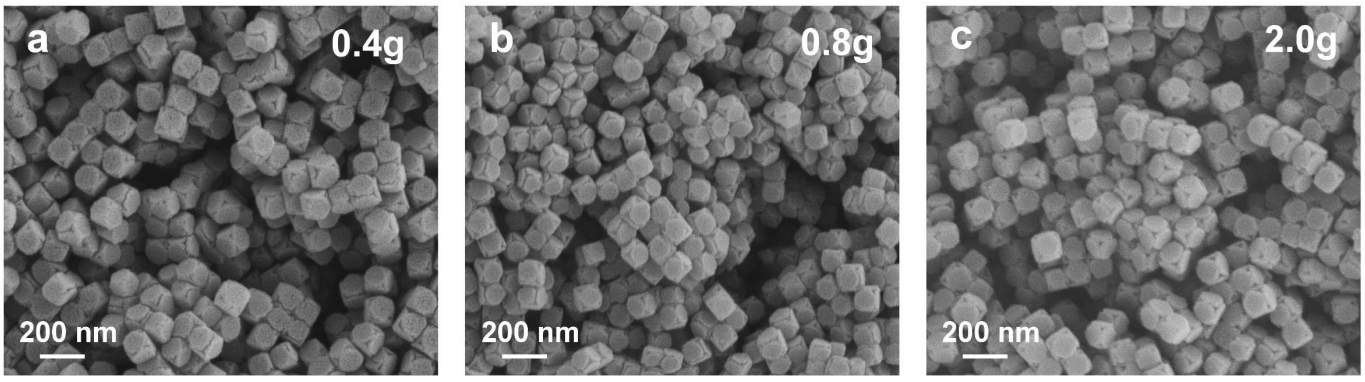

Figure S1 (a-c) SEM images of NiCoHCF octa-truncated cubes treated with different concentrations of ammonium oxalate at 90 °C for 1h.

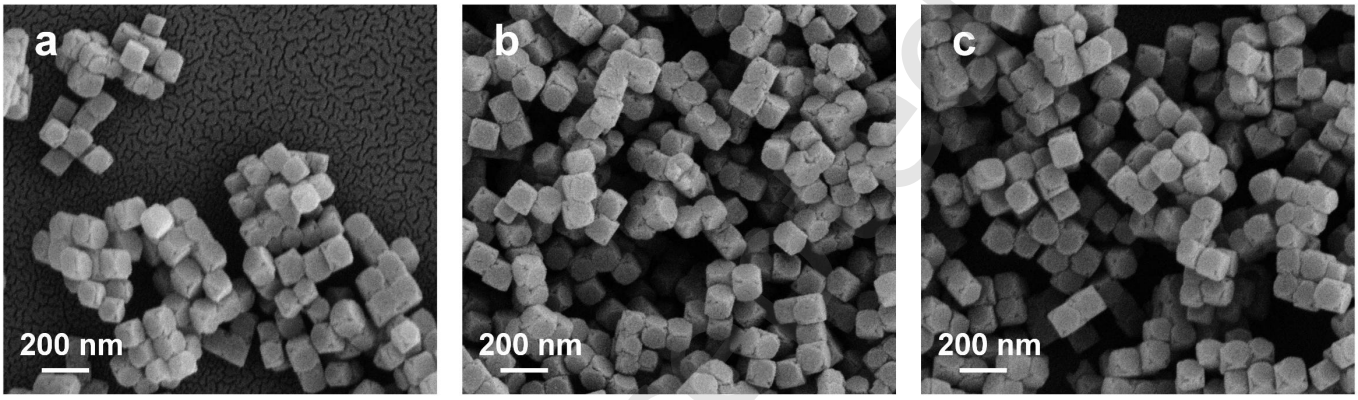

Figure S2 SEM images of NiCoHCF octa-truncated cubes treated with 0.2 g of ammonium oxalate at 90 °C for (a) 0.5 h, (b) 3 h, (c) 6 h.

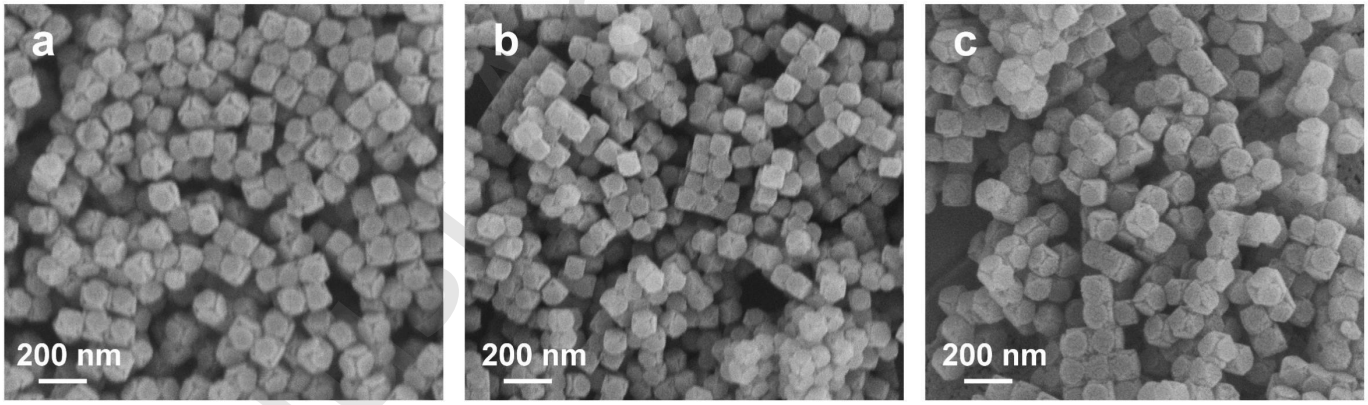

Figure S3 SEM images of NiCoHCF octa-truncated cubes treated with 1.2 g of ammonium oxalate at 90 °C for (a) 0.5 h, (b) 3 h, (c) 6 h.

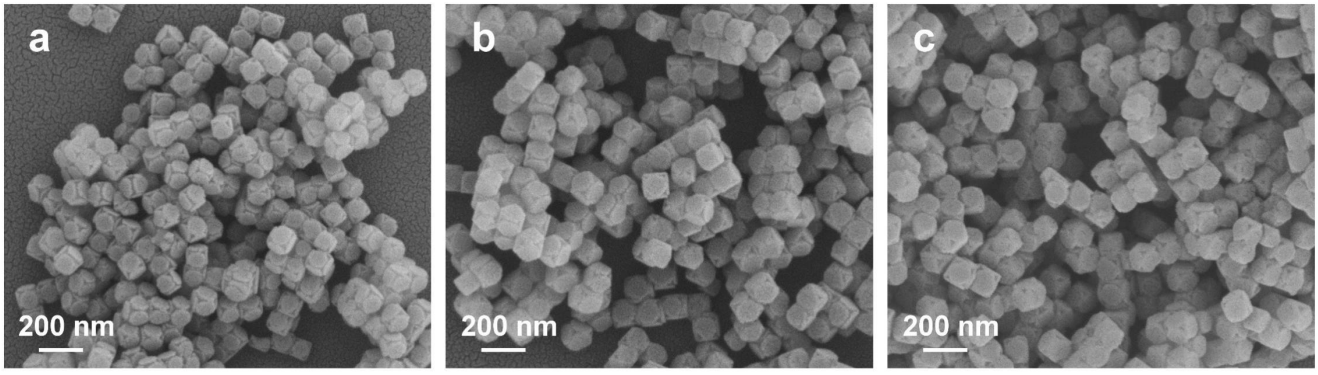

Figure S4 SEM images of NiCoHCF octa-truncated cubes treated with 1.6 g of ammonium oxalate at 90 °C for (a) 0.5 h, (b) 3 h, (c) 6 h.

Figure S5 SEM images of NiCoHCF octa-truncated cubes treated with 1.2 g of ammonium oxalate at room temperature for (a) 0.5 h, (b) 1 h, (c) 3 h, (d) 6 h.

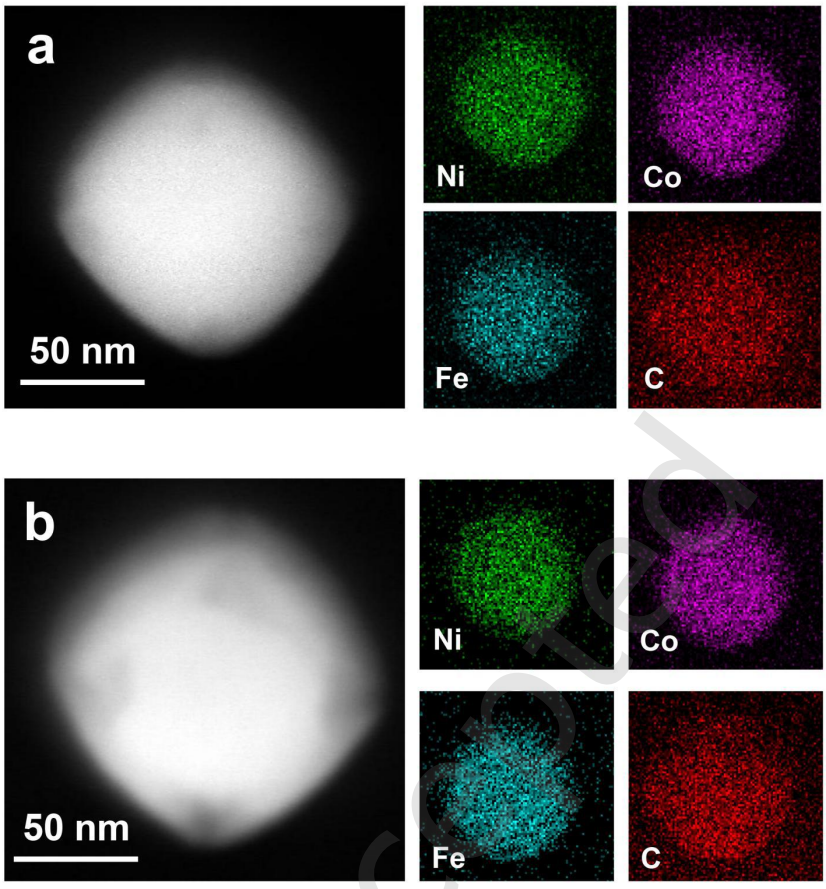

Figure S6 HAADF-STEM image and corresponding elemental mapping images of (a) NiCoHCF-0.2 and (b) NiCoHCF-1.6.

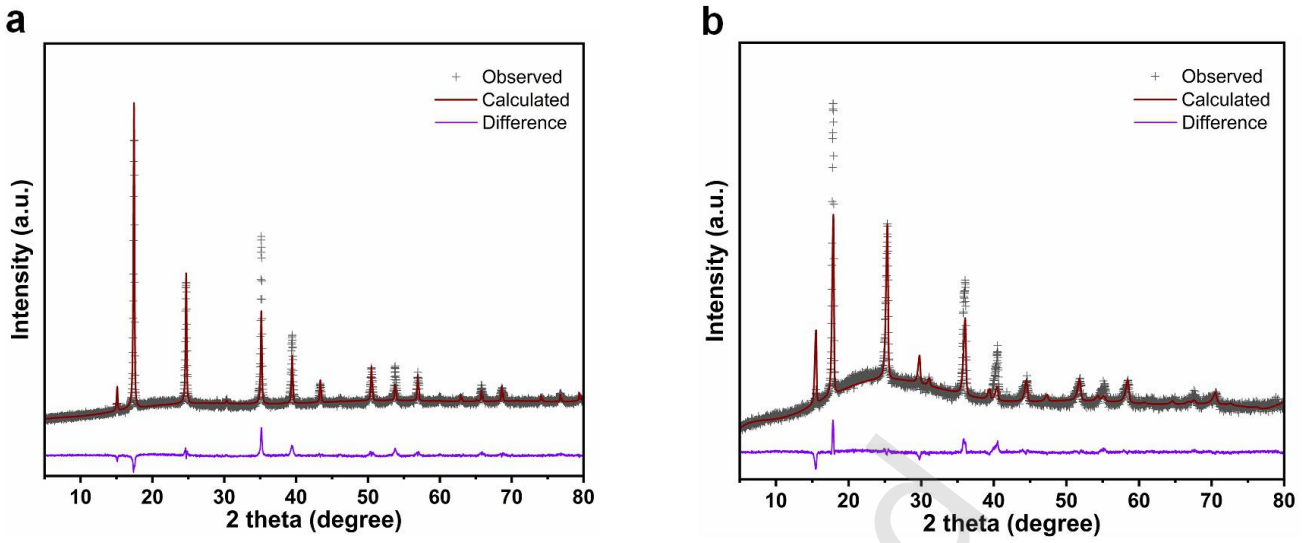

Figure S7 Rietveld refinement of NiCoHCF and NiCoHCF-1.2.

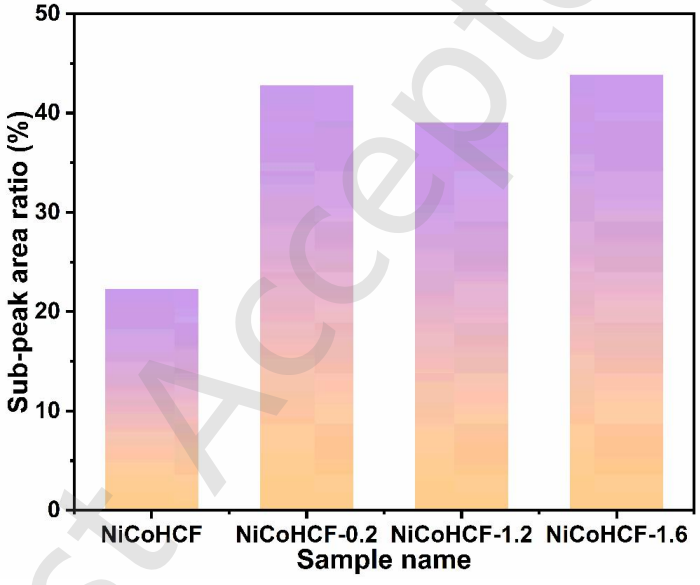

Figure S8 C≡N peak area ratios of NiCoHCF and NiCoHCF-X (X = 0.2,1.2,1.6).

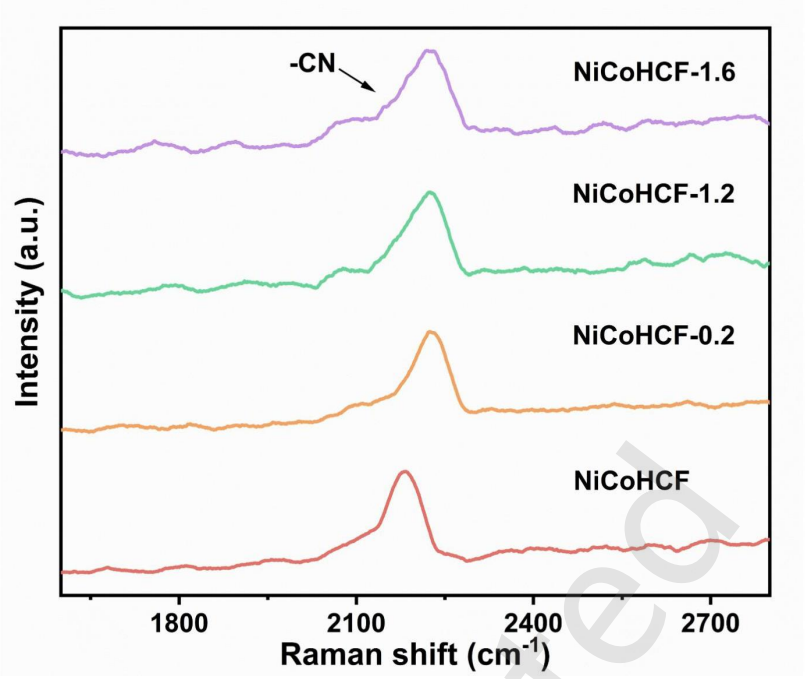

Figure S9 Raman spectra of NiCoHCF and NiCoHCF-X (X = 0.2,1.2,1.6).

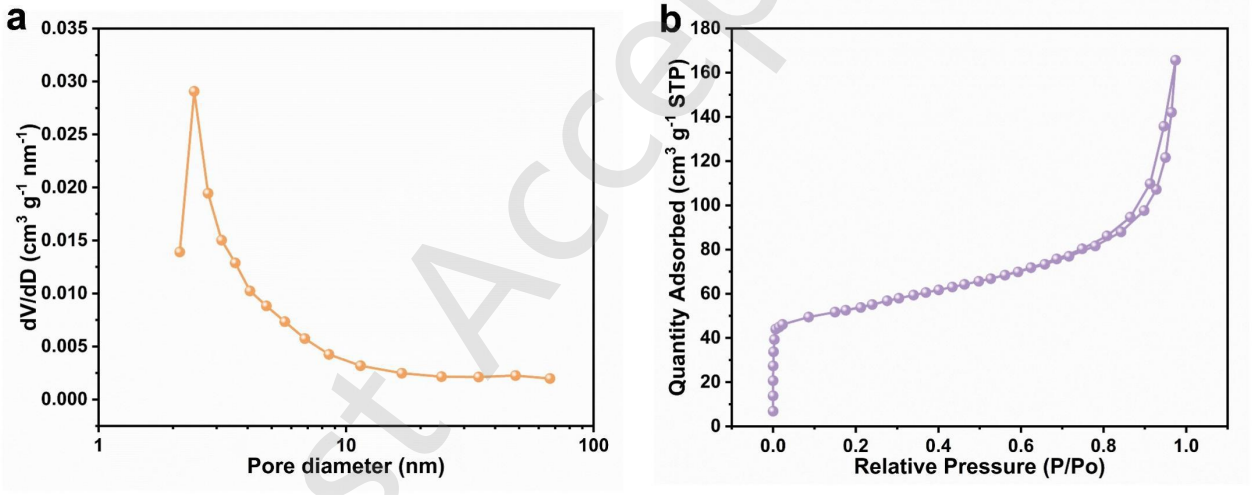

Figure S10 (a) N_2 adsorption-desorption isotherms of NiCoHCF. (b) Pore size distribution plots of NiCoHCF.

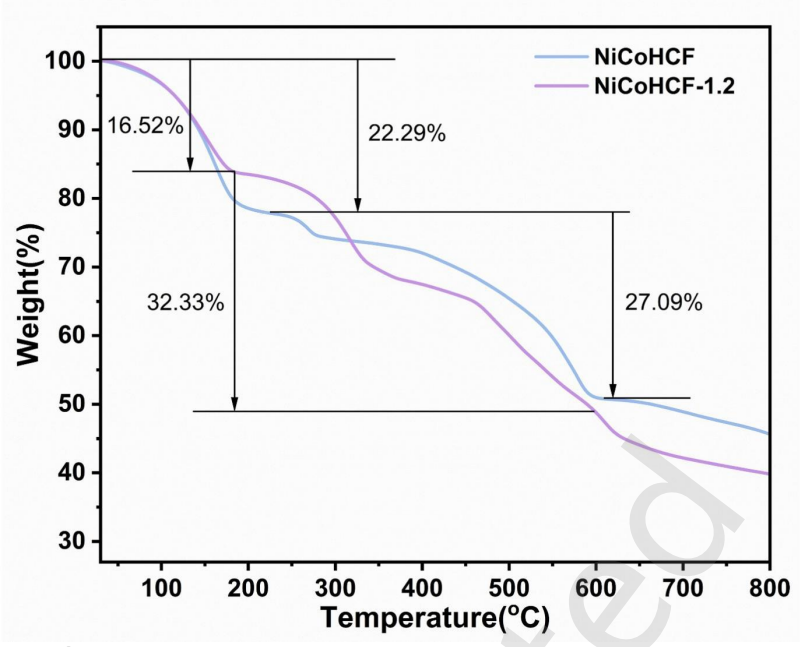

Figure S11 TGA curve of NiCoHCF and NiCoHCF-1.2.

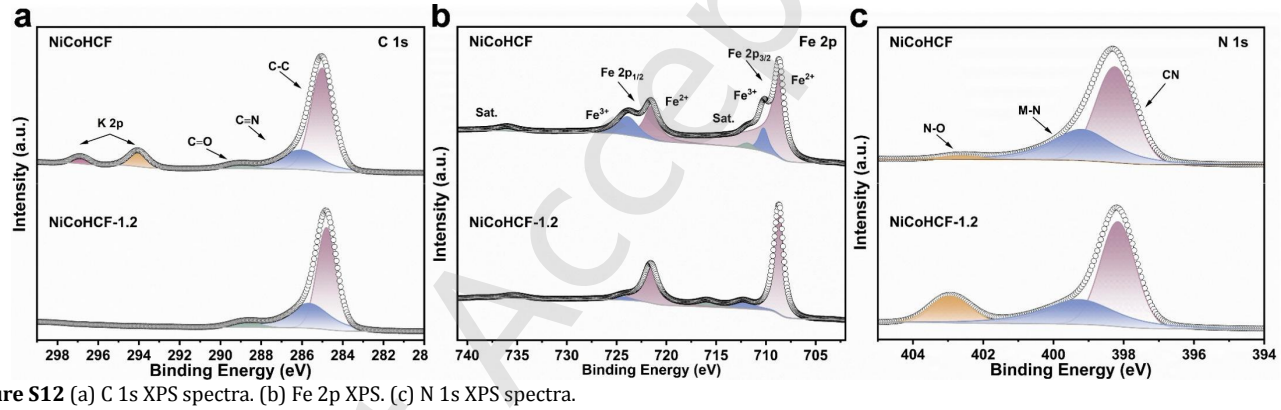

Figure S12 (a) C 1s XPS spectra. (b) Fe 2p XPS. (c) N 1s XPS spectra.

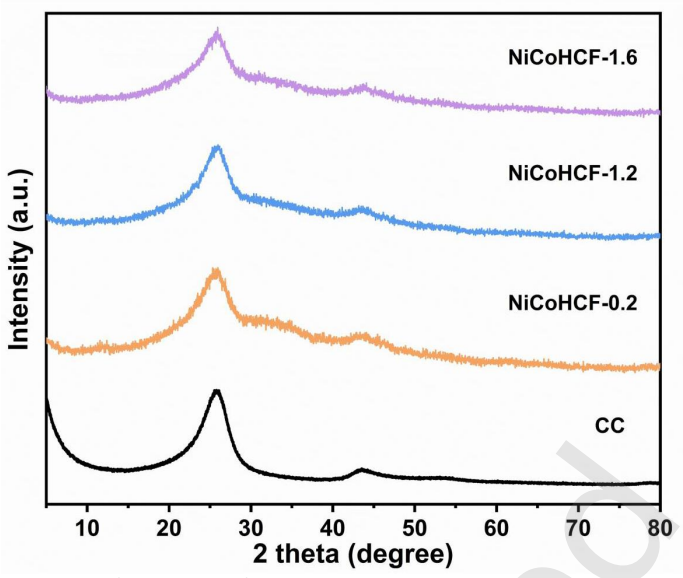

Figure S13 XRD pattern of the CC and NiCoHCF-X (X = 0.2,1.2,1.6).

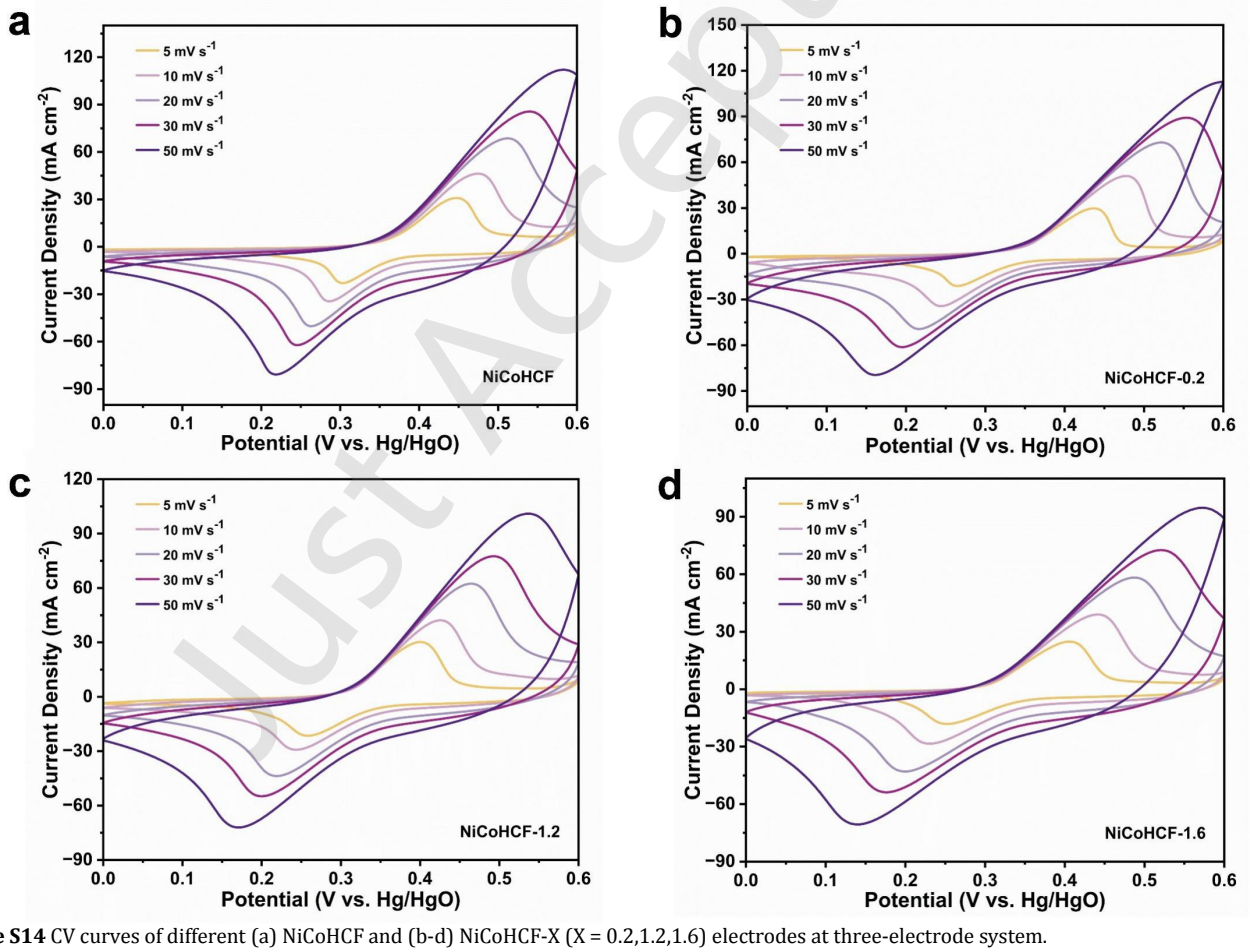

Figure S14 CV curves of different (a) NiCoHCF and (b-d) NiCoHCF-X (X = 0.2,1.2,1.6) electrodes at three-electrode system.

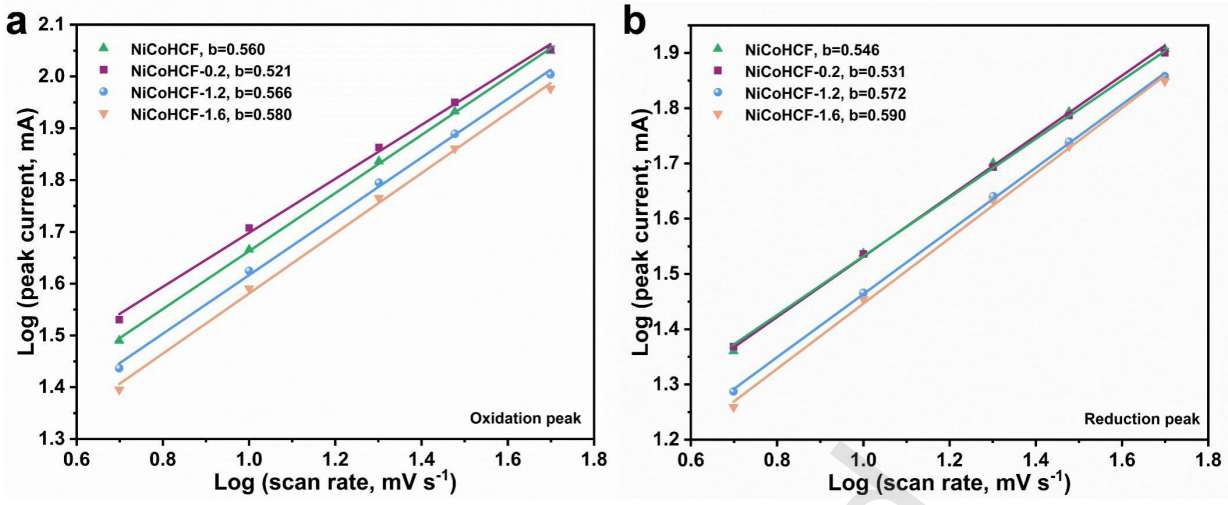

Figure S15 The plots of log (peak current) against log (scan rate) for different electrodes. (a) oxidation peak, (b) reduction peak.

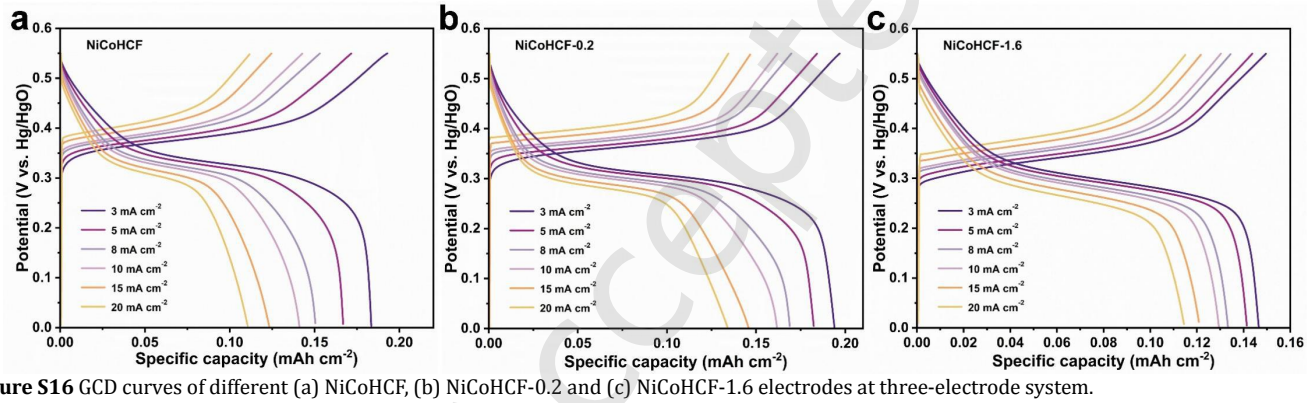

Figure S16 GCD curves of different (a) NiCoHCF, (b) NiCoHCF-0.2 and (c) NiCoHCF-1.6 electrodes at three-electrode system.

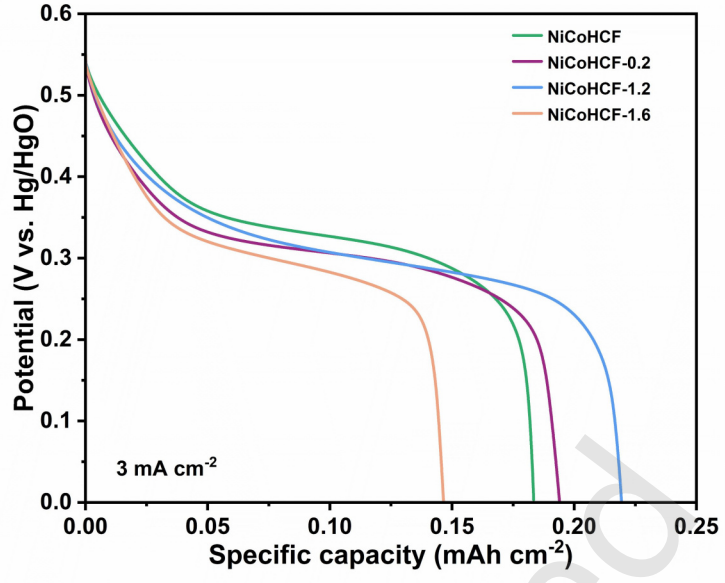

Figure S17 GCD prodiles of NiCoHCF and NiCoHCF-X at 3 mA/cm^2.

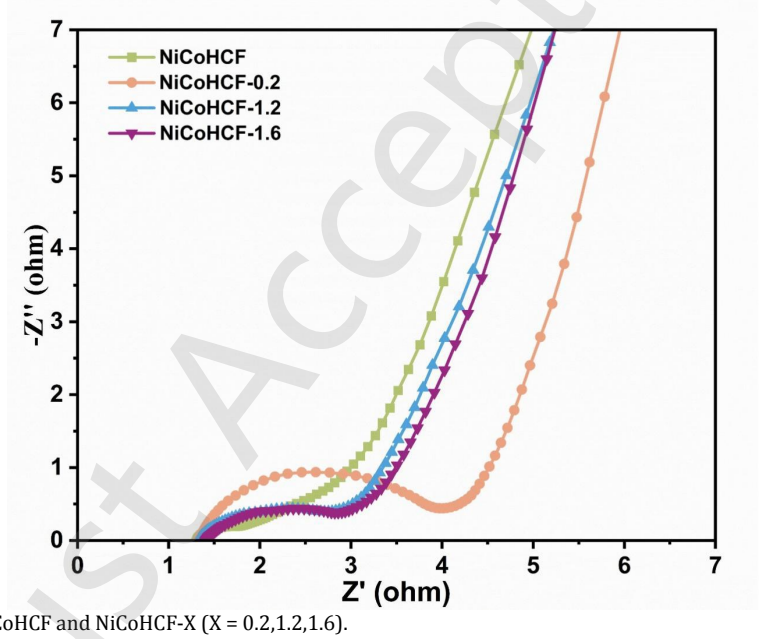

Figure S18 EIS pattern of the NiCoHCF and NiCoHCF-X (X = 0.2,1.2,1.6).

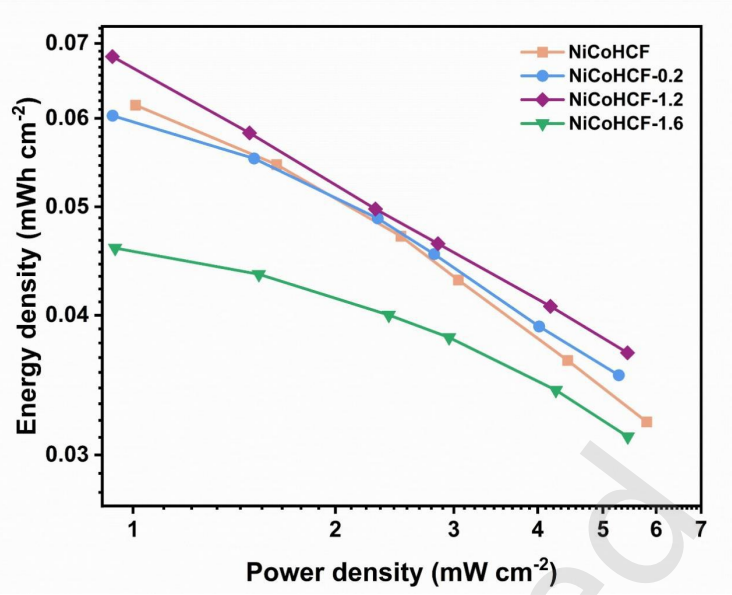

Figure S19 Ragone plot based on areal energy/power density.

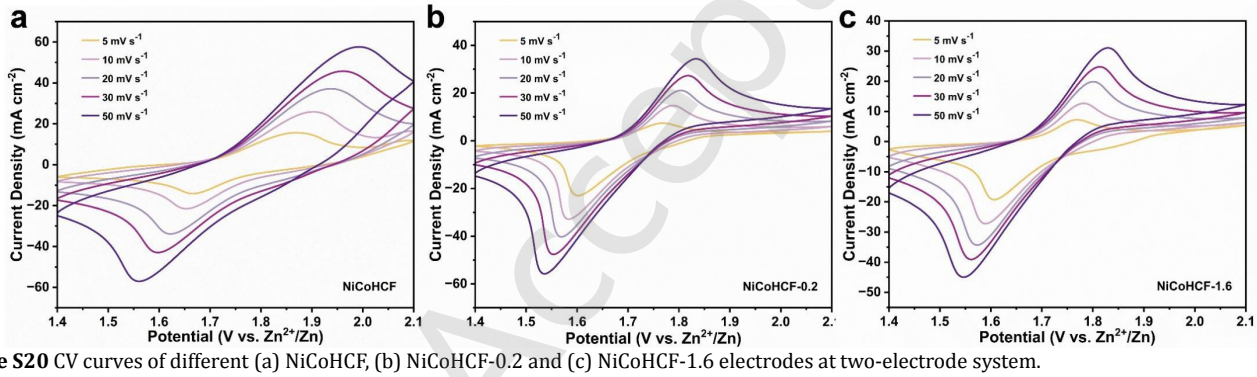

Figure S20 CV curves of different (a) NiCoHCF, (b) NiCoHCF-0.2 and (c) NiCoHCF-1.6 electrodes at two-electrode system.

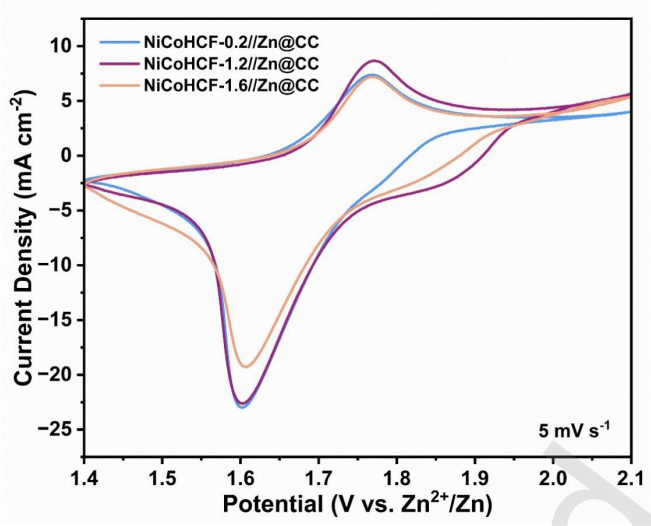

Figure S21 CV curves of NiCoHCF-X (X = 0.2,1.2,1.6) electrodes at 5 mv s^{-1} in two-electrode system.

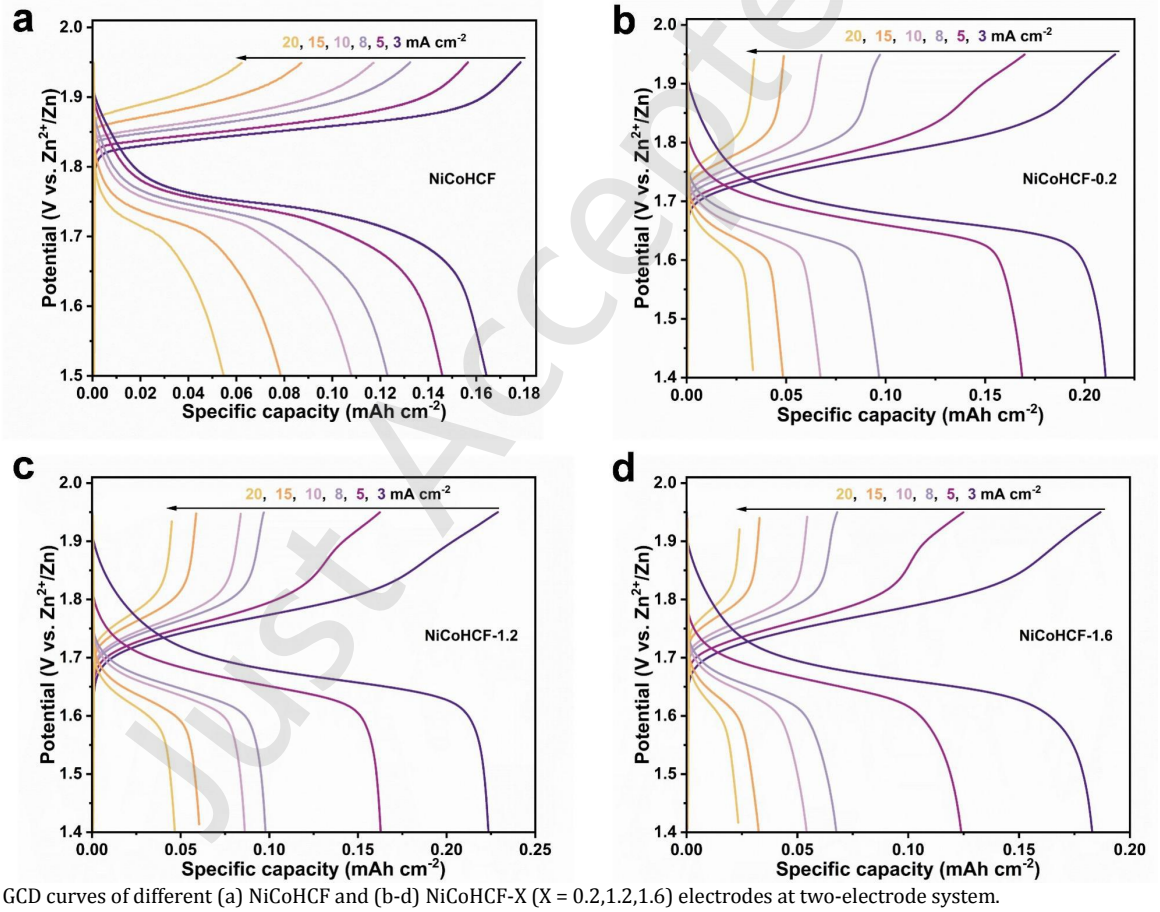

Figure S22 GCD curves of different (a) NiCoHCF and (b-d) NiCoHCF-X (X = 0.2,1.2,1.6) electrodes at two-electrode system.

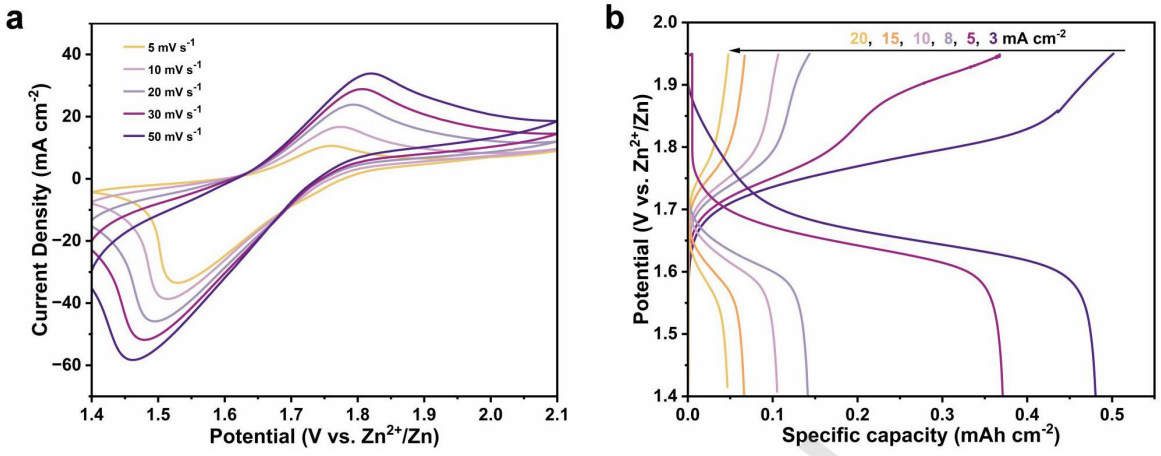

Fig S23 (a) CV and (b) GCD curves of the NiCoHCF-1.2 electrode (mass loading ≥10 mg cm^{-2}) at two-electrode system.

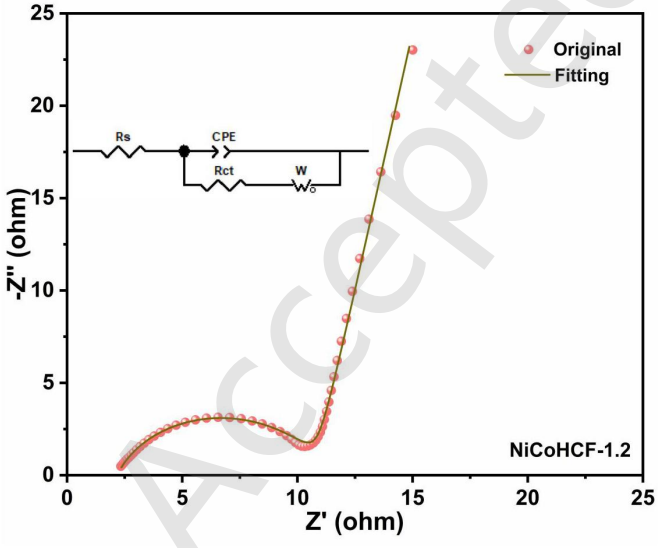

Fig S24 EIS fitting spectra of NiCoHCF-1.2.

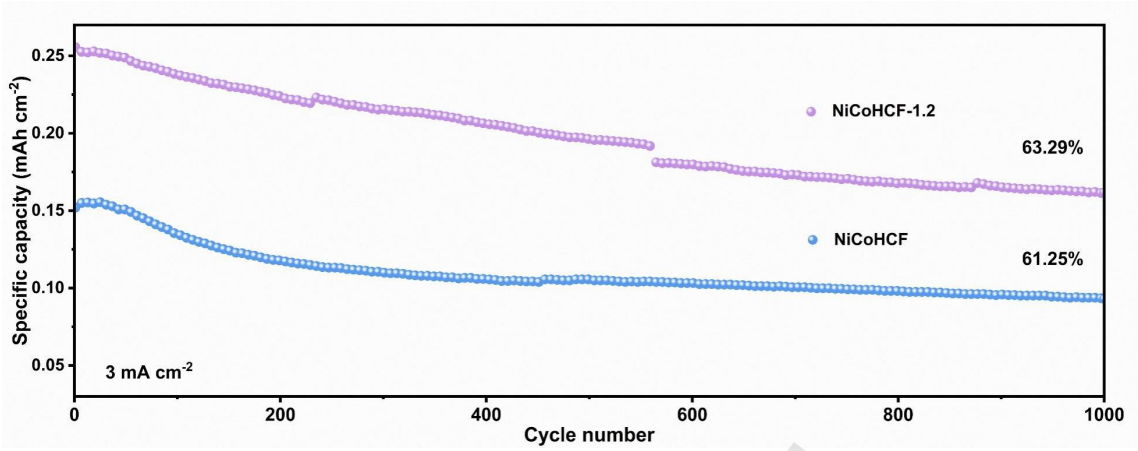

Figure S25 Cycling stability of the NZBs cells at 3 mA cm^{-2}.

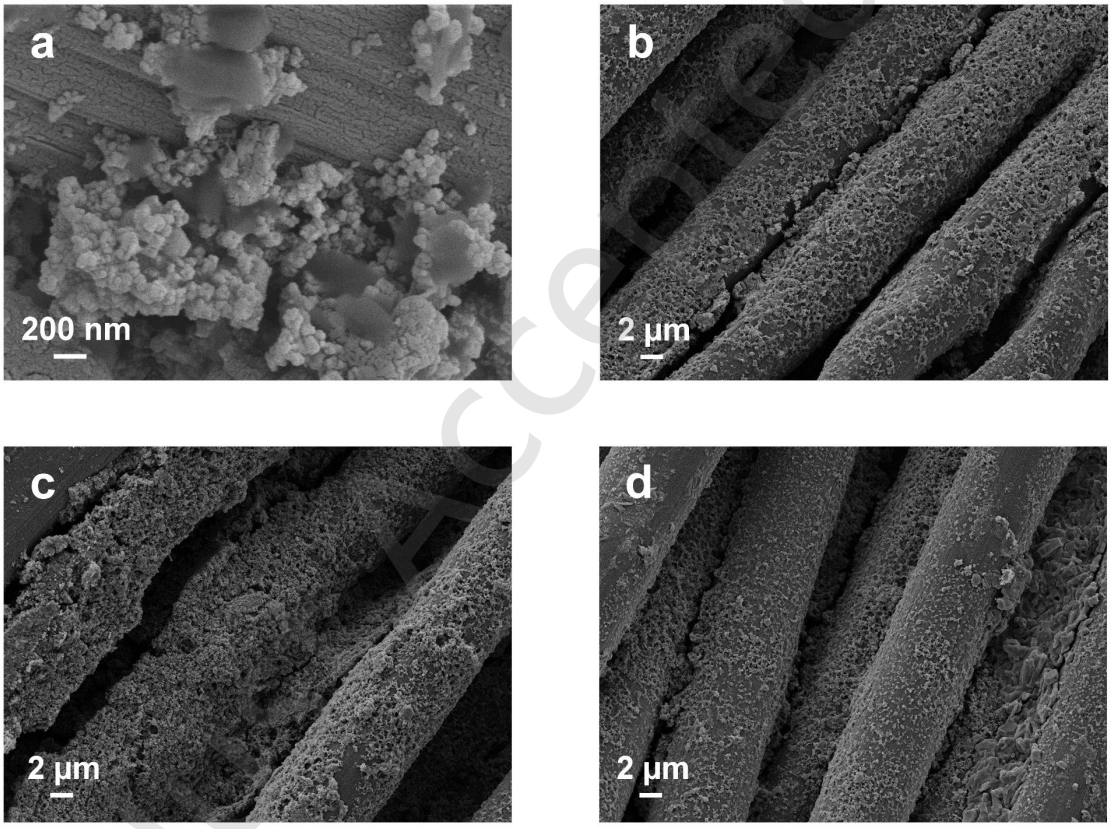

Figure S26 SEM images of (a) NiCoHCF and (b-d) NiCoHCF-X (X = 0.2,1.2,1.6) electrodes after two-electrode system tests.

Table S1 The peak positions and of deconvoluted Co 2p, Ni 2p and Fe 2p spectra of NiCoHCF and NiCoHCF-1.2.

Samples		NiCoHCF	B.E.(eV)	NiCoHCF-1.2	B.E.(eV)
Ni^{3+}/Ni^{2+}	Ni $2p_{3/2}$	856.44/859.49		856.33/858.84	
	Ni $2p_{1/2}$	873.79/876.07		873.79/880.70	
Co^{3+}/Co^{2+}	Co $2p_{3/2}$	782.30/785.47		782.35/785.75	
	Co $2p_{1/2}$	797.72/801.18		797.62/802.32	
Fe^{3+}/Fe^{2+}	Fe $2p_{3/2}$	708.67/710.21		708.66/712.29	
	Fe $2p_{1/2}$	721.52/723.88		721.56/724.28	

Table S2 Comparison of energy densities between NiCoHCF-1.2//Zn@CC cell with other previously reported works.

Electrode materials	E_A [a] (mWh cm^{-2})	E_A at max power density (mWh cm^{-2}/ mW cm^{-2})	References
NiCoFe-PBA/MOF-2	0.22	1.73	[2]
MOCF	0.033	0.11	[3]
Ni-OA-3	0.42	5.36	[4]
NiCo-MOF/NiO-150//AC	0.0187	2.4	[5]
Co-CH@NiAl-LDH/CC//PPC	0.27	2.83	[6]
PPy@NiCo-LDH@ITO	0.0547	0.5	[7]
Ni-Co-P@LDH//FeOOH	0.000654	0.1	[8]
CuZn-MOF-P7	0.0223	6.75	[9]
Ni–NiO//Zn	0.0066	20.2	[10]
NiCoHCF-1.2	**0.38**	**31.84**	**This work**

a) E_A: areal energy density.

Table S3 Comparison of cycling performance NiCoHCF-1.2//Zn@CC cell with other previously reported works.

Electrode materials	Cycling performance	References
NiCoFe-PBA/MOF-2//Zn	57 % after 1000 cycles at 3 mA cm^{-2}	[2]
SNZO//Zn	65.2 % after 1800 cycles at 1 mA cm^{-2}	[11]
NiCoFe-PBA-3//Zn	51 % after 1000 cycles at 3 mA cm^{-2}	[12]
Ni-MOF//Zn	89 % after 600 cycles at 1 mA cm^{-2}	[13]
SCNF@Ni@MOF@NiCo LDHs//Zn	55 % after 5000 cycles at 2.5 mA cm^{-2}	[14]
Ni-mMeSA // Zn	44.2 % after 1000 cycles at 5 mA cm^{-2}	[15]
NiCoHCF-1.2//Zn	**63 % after 1000 cycles at 3 mA cm^{-2}**	**This work**

References

[1] Huang, J.; Xiong, Y.; Peng, Z.; Chen, L.; Wang, L.; Xu, Y.; Tan, L.; Yuan, K.; Chen, Y. A general electrodeposition strategy for fabricating ultrathin nickel cobalt phosphate nanosheets with ultrahigh capacity and rate performance. *ACS Nano* **2020,** *14*, 14201-14211.

[2] Pi, Y.; Lin, H.; Meng, Z.; Qiu, Z.; Su, Y.; Hang, X.; Pang, H. Self-template synthesis of PBA/MOF hollow nanocubes for aqueous battery. *Chem. Eng. J.* **2024,** *499,* 155618.

[3] Wang, L.; Liu, R. Knitting controllable oxygen-functionalized carbon fiber for ultrahigh capacitance wire-shaped supercapacitors. *ACS Appl. Mater. Interfaces* **2020,** *12*, 44866-44873.

[4] Sun, F.; Chen, T.; Li, Q.; Pang, H. Hierarchical nickel oxalate superstructure assembled from 1D nanorods for aqueous nickel-zinc battery. *J. Colloid Interface Sci.* **2022,** *627*, 483-491.

[5] Nan, W.; Li, Y.; Zhang, J.; Wang, F.; Liu, X.; Chen, Z.; Xiang, J.; Savilov, S. V.; Sobolev, A. V.; Wang, L.; Li, Z.; Chen, M. Nano-thin heterogeneous NiCo MOF/NiO nanosheets for high-rate energy storage. *Surf. Coat. Technol.* **2025,** *497*, 131781.

[6] Wang, Y.; Jiang, D.; Zhang, Y.; Chen, J.; Xie, M.; Du, C.; Wan, L. Controlled preparation of cobalt carbonate hydroxide@nickel aluminum layered double hydroxide core-shell heterostructure for advanced supercapacitors. *J. Colloid Interface Sci.* **2024,** *654*, 379-389.

[7] Li, X.; Wang, X.; Liu, G.; Sui, X.; Wu, Q.; Wang, X.; Lv, X.; Xie, E.; Zhang, Z. 2.5 V "water in salt" aqueous micro-supercapacitors based on polypyrrole-coated NiCo layered double hydroxides. *Chem. Eng. J.* **2023,** *452*, 139140.

[8] Zhan, J.; Yang, H.; Zhang, Q.; Zong, Q.; Du, W.; Wang, Q. Multi-step electrodeposited Ni-Co-P@LDH nanocomposites for high-performance interdigital asymmetric micro-supercapacitors. *Dalton Trans.* **2022,** *51*, 6242-6253.

[9] Aashi; Rani, R.; Alagar, S.; Sharma, J.; k, A.; Bagchi, V. Laser-induced crafting of modulated structural defects in MOF-based supercapacitor for energy storage application. *ACS Mater. Lett.* **2024,** *6*, 1769-1778.

[10] Zeng, Y.; Meng, Y.; Lai, Z.; Zhang, X.; Yu, M.; Fang, P.; Wu, M.; Tong, Y.; Lu, X. An ultrastable and high‐performance flexible fiber‐shaped Ni-Zn battery based on a Ni-NiO heterostructured nanosheet cathode. *Adv. Mater.* **2017,** *29*, 1702698.

[11] Zhang, X.; Noréus, D. Selenized Zn-doped $NiMoO_4$ modified with the prussian blue analogue as electrodes for aqueous alkaline NiZn batteries. *Chem. Eng. J.* **2025**, *519*, 165666.

[12] Jiang, Z.; Zhang, S.; Wang, S.; Qiu, Z.; Lin, H.; Li, Q.; Cao, S.; Xu, Y.; Pi, Y.; Pang, H. Design of iron-based prussian blue analogues via transition metal incorporation for aqueous Ni-Zn batteries. *Rare Met.* **2025**, *44*, 10998-11005.

[13] Li, C.; Zhang, Q.; Li, T.; He, B.; Man, P.; Zhu, Z.; Zhou, Z.; Wei, L.; Zhang, K.; Hong, G.; Yao, Y. Nickel metal-organic framework nanosheets as novel binder-free cathode for advanced fibrous aqueous rechargeable Ni-Zn battery. *J. Mater. Chem. A* **2020**, *8*, 3262-3269.

[14] Xia, Z.; Pan, J.; Chen, H.; Deng, N.; Yang, C.; Liu, X.; Liu, Y.; Wu, L. Flexible one-dimensional yarn-like Ni-Zn battery: micron-nano hierarchical-structure array, high energy density and excellent capacity retention. *Chem. Eng. J.* **2023**, *456*, 141048.

[15] Su, Y.; Hu, J.; Yuan, G.; Zhang, G.; Wei, W.; Sun, Y.; Zhang, X.; Liu, Z.; Suen, N. T.; Chen, H. C.; Pang, H. Regulating intramolecular electron transfer of nickel-based coordinations through ligand engineering for aqueous batteries. *Adv. Mater.* **2023**, *35,* 2307003.